iScience

CellPress
OPEN ACCESS

Article

Dynamics of nuclear export of pre-ribosomal subunits revealed by high-speed single-molecule microscopy in live cells

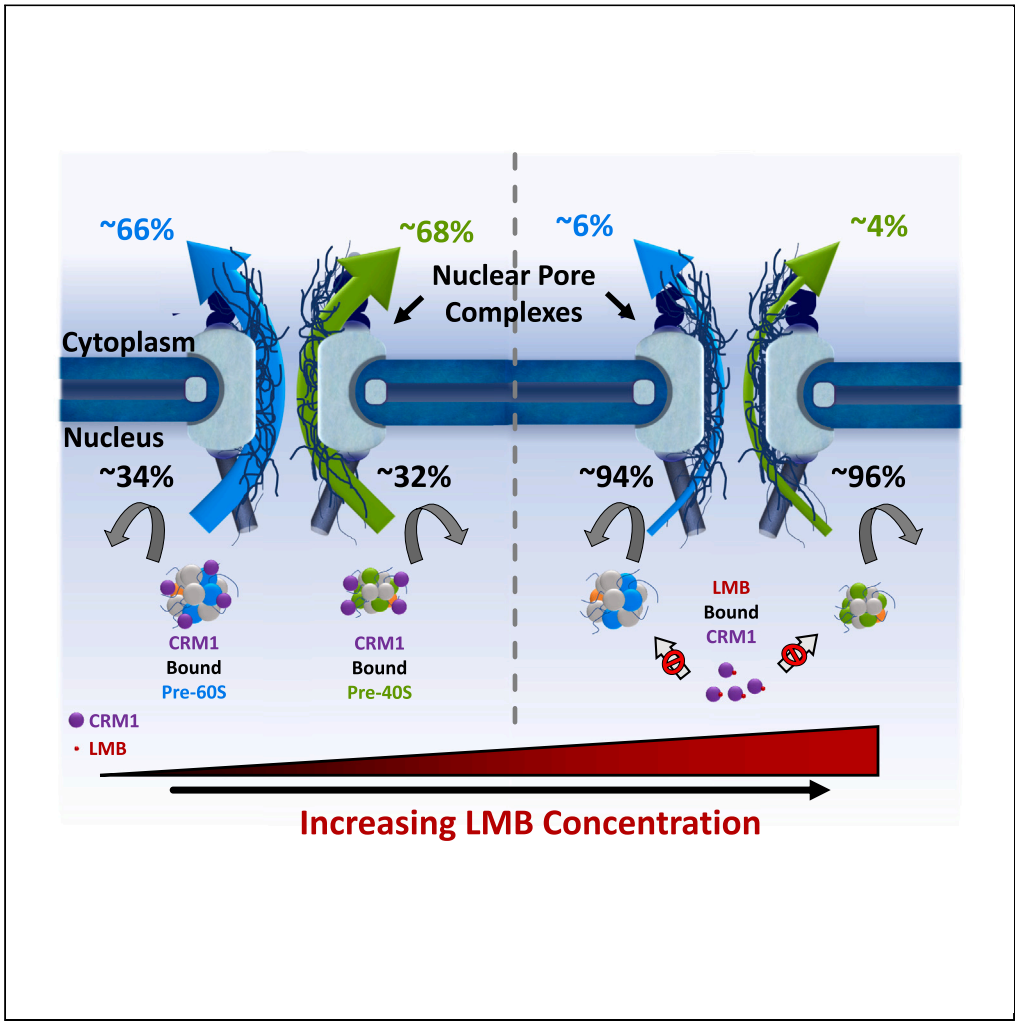

Samuel L. Junod, Mark Tingey, Joseph M. Kelich, Alexander Goryaynov, Karl Herbine, Weidong Yang

weidong.yang@temple.edu

Highlights

Pre-ribosomal particles exhibit high nuclear export efficiency in live cells

CRM1 inhibition leads to a significant decrease in pre-ribosome nuclear export

Multiple CRM1s may cooperatively export pre-ribosome particles

Junod et al., iScience *26*, 107445
August 18, 2023
https://doi.org/10.1016/j.isci.2023.107445

iScience

CellPress
OPEN ACCESS

Article

Dynamics of nuclear export of pre-ribosomal subunits revealed by high-speed single-molecule microscopy in live cells

Samuel L. Junod,[1] Mark Tingey,[1] Joseph M. Kelich,[1] Alexander Goryaynov,[1] Karl Herbine,[1] and Weidong Yang[1,2,*]

SUMMARY

We present a study on the nuclear export efficiency and time of pre-ribosomal subunits in live mammalian cells, using high-speed single-molecule tracking and single-molecule fluorescence resonance energy transfer techniques. Our findings reveal that pre-ribosomal particles exhibit significantly higher nuclear export efficiency compared to other large cargos like mRNAs, with around two-thirds of interactions between the pre-60S or pre-40S and the nuclear pore complexes (NPCs) resulting in successful export to the cytoplasm. We also demonstrate that nuclear transport receptor (NTR) chromosomal maintenance 1 (CRM1) plays a crucial role in nuclear export efficiency, with pre-60S and pre-40S particle export efficiency decreasing by 11–17-fold when CRM1 is inhibited. Our results suggest that multiple copies of CRM1 work cooperatively to chaperone pre-ribosomal subunits through the NPC, thus increasing export efficiency and decreasing export time. Significantly, this cooperative NTR mechanism extends beyond pre-ribosomal subunits, as evidenced by the enhanced nucleocytoplasmic transport of proteins.

INTRODUCTION

Ribosome biogenesis begins in the nucleolus with the formation of a pre-90S ribosome. This is then followed by a division into two daughter subunits, the pre-60S and pre-40S. These pre-ribosomal subunits then transition from the nucleolus to the nucleoplasm, by associating with various ribosomal proteins (RPs or r-proteins) and assembly factors along the way.[1–3] At the time of nuclear export, the pre-60S and pre-40S are among the largest endogenous molecules to transport across the nuclear envelope (NE) and will have a molecular weight and diameter of ~2.5 MDa; ~25 nm and ~1.4 MDa; ~16 nm, respectively.[4–7]

The primary factor regulating import and export from the nucleus is the nuclear pore complex (NPC).[8–11] The structure embedded in the NE serves as a gateway for all import and export processes, including the transportation of pre-60S and pre-40S pre-ribosomal subunits. The NPC is a megadalton structure comprised approximately 30 different proteins, known as nucleoporins (Nups), with each Nup containing between 8 and 32 copies in an 8-fold radial stoichiometry.[12,13] Approximately one-third of these Nups contain intrinsically disordered regions rich in phenylalanine-glycine (FG) repeats.[14–16] These FG-Nups work together to create a hydrophobically dense environment that acts as a selectivity barrier for transiting molecules,[16–22] with the greatest concentration of FG repeats located in the internal periphery of the central scaffold region.[23] Smaller molecules (<40–60 kDa, < ~8 nm diameter) are known to passively diffuse through the central channel of the NPC, whereas larger molecules (>60 kDa, > ~8 nm diameter) are selectively inhibited.[17–22] However, molecules such as the pre-60S and pre-40S subunits can overcome this selective inhibition through facilitated diffusion, which involves the assistance of nuclear transport receptors (NTRs).

Facilitated diffusion of cargo by NTRs requires the presence of a nuclear localization signal (NLS) or a nuclear export signal (NES) on the cargo. In mammalian cells, three major NTRs are associated with the pre-60S subunit. Chromosomal region maintenance 1 (CRM1) was the first identified transport receptor for pre-60S particles, and it promotes the export of cargoes containing leucine-rich NESs.[24,25] CRM1 interacts with

[1]Department of Biology, Temple University, Philadelphia, PA, USA

[2]Lead contact

*Correspondence: weidong.yang@temple.edu

https://doi.org/10.1016/j.isci.2023.107445

almost all FG-Nups in the NPC and is dissociated during the small GTPase Ran cycle at the cytoplasmic end of the pore.[24–26] Additionally, CRM1 recognizes pre-60S complexes via the NES signal carried by Nmd3, an export adaptor protein incorporated into the pre-60S complex.[26] Another factor, Rrp12p, is a nuclear export factor that interacts with several FG-Nups and utilizes the RanGTP cycle to facilitate the export of pre-60S particles through the NPC. Lastly, the Tap-p15 heterodimer (known as Mex67p-Mtr2p in yeast) may contribute to the translocation of pre-60S particles through the NPC and acts independently of the RanGTPase cycle.[27,28] However, while Tap-p15 has been implicated, there is little direct evidence for it directly contributing to the export of pre-ribosomal subunits. Compared to pre-60S particles, fewer studies have investigated the nuclear export of pre-40S particles, but Rio2 has been reported to contribute to their export in human cells.[29] In yeast, CRM1 is considered the major transport receptor for exporting pre-40S particles through the NPC, while Rrp12 is a major export factor.[30–32] Ltv1p and DIM2 also function as an adapter for CRM1 recruitment in pre-40S export.[31] Several studies have identified CRM1 as a major transport receptor for both pre-ribosomal subunits; however, none have quantified the molecular-level consequences of inhibiting CRM1-dependent nuclear export for these particles.

Pre-ribosomal subunit export from the nucleus through the NPC has been studied extensively in biochemical and structural analyses.[5,6,30,31,33–37] However, due to the multifunctional roles of r-proteins outside of the ribosome, it is difficult to examine the transport kinetics of pre-ribosomal subunits within mammalian NPCs.[38,39] Therefore, a method for tracking intact pre-ribosomal subunits in nucleocytoplasmic export is necessary to develop a more specific understanding of their behaviors. In this study, high-speed single-molecule microscopy combined with fluorescence resonance energy transfer (FRET) was used to visualize single intact pre-60S and pre-40S subunits as they interacted with NPCs in live cells. This approach excluded dynamic information resulting from r-protein behaviors outside the scope of export and specific interactions with NTRs at the NPC, providing highly specific information regarding only the dynamics of export.

Our studies showed that about two-thirds of pre-60S or pre-40S subunits interacting with NPCs successfully exported from the nucleus. Additionally, inhibiting CRM1-dependent pre-60S and pre-40S nuclear export directly revealed, for the first time, the impact of CRM1 on pre-ribosomal export, demonstrating a 10–17-fold decrease in export efficiency of pre-60S and pre-40S particles when CRM1 is inhibited. This provided significant insight into the role of CRM1 in the export of pre-ribosomal subunits and how large complexes can export with high efficiency. Furthermore, single-molecule trajectories of pre-ribosomal subunits further indicate high probability of completing nuclear export after passing through the nuclear basket and NPC center, which serve as selectivity barriers for these particles. This enabled us to propose a model for the nuclear export of pre-60S and pre-40S subunits, in which multiple copies of CRM1 work cooperatively to chaperone pre-ribosomal subunits overcoming these barriers, thus increasing export efficiency and decreasing export time. Expanding this study to quantify nucleocytoplasmic kinetics for other large cargoes such as viral capsids, proteasome components, and synthetic vectors for drug or gene therapy delivery in various cell systems is of interest. This could provide valuable insights into the general mechanisms of nuclear transport beyond pre-ribosomal particles and could potentially have significant implications for drug and gene therapy development.

RESULTS

Microscopy setup, labeled pre-ribosomal particles, and identified nuclear export signals

To capture single molecules transporting through the sub-micrometer regions of the NPC, single-point edge-excitation sub-diffraction (SPEED) microscopy was utilized.[19,20] SPEED microscopy was designed to image a single NPC from neighboring NPCs in live cells with either an inclined or a vertical illumination patterns in the focal plane[40,41] (Figures 1A–1E). This unique microscopy method facilitates the collection of dynamic information for molecules transiting through biological channels and cavities with rotational symmetry at high spatiotemporal resolutions of $\lesssim$10–20 nm and 0.4–2 ms.[22,41–44] Optical lenses can be inserted on the optical path of excitation light to convert the microscopy imaging from SPEED mode to narrow-field fluorescence microscopy (Figure 1B). Single-molecule FRET (smFRET) measurements were conducted in either SPEED or narrow-field mode by collecting the FRET signal from a donor-acceptor fluorophore pair (Figures 1A, 1C, and 1F–1I).

A novel labeling strategy was employed to resolve and isolate intact pre-60S and pre-40S particles from single r-proteins interacting with single NPCs. The objective was to ensure that the particle being tracked is indeed assembled pre-ribosomal subunits and not lone r-proteins or contaminated irrelevant protein

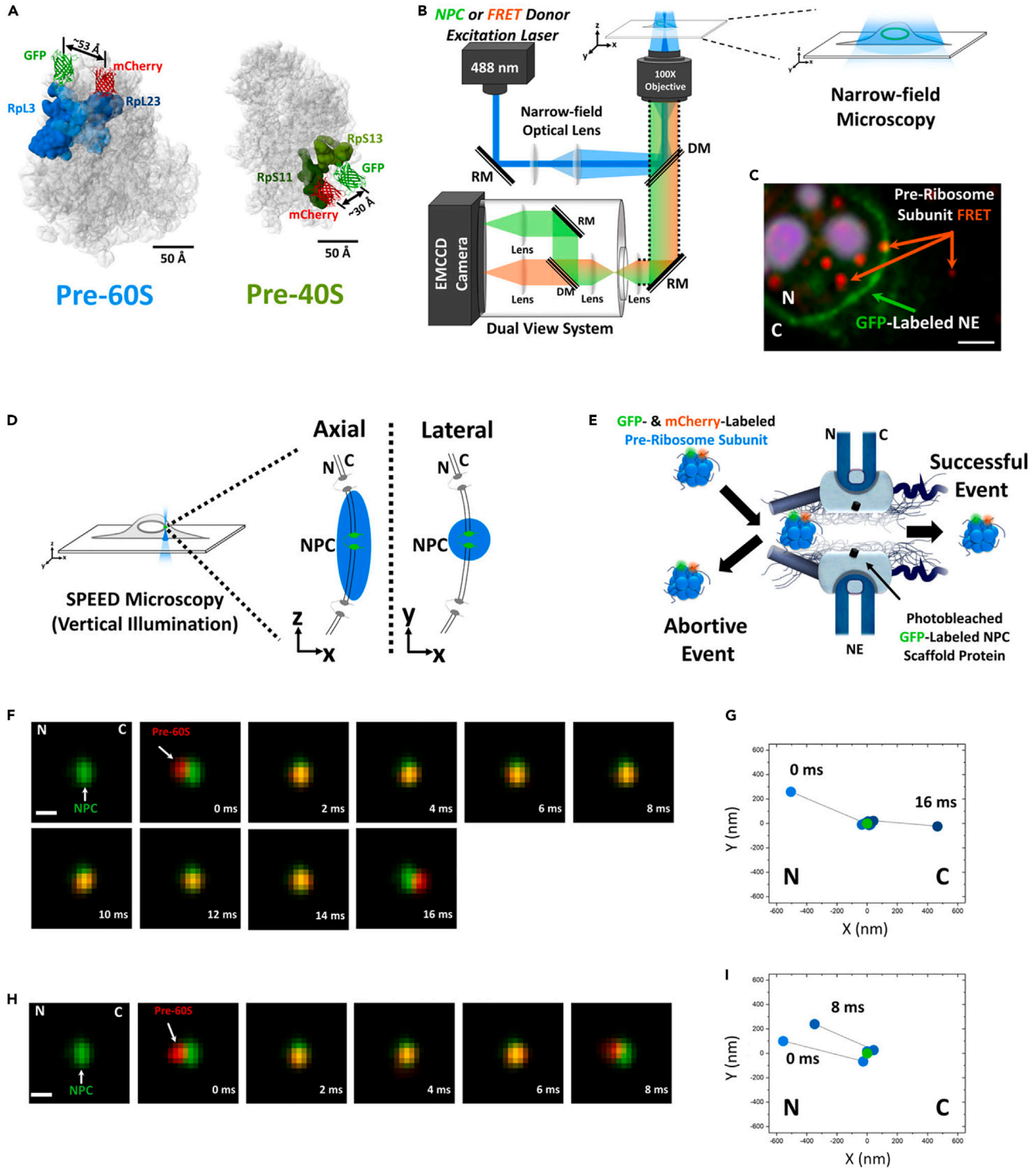

Figure 1. Experimental Setup for tracking single pre-ribosomal subunits through the NPC

(A) The structures of the pre-60S (left, PDB: 6LU8) and pre-40S (right, PDB: 6G4S) are displayed based on previous cryo-EM studies, indicating the relative distance between the FRET pair utilized. GFP (green) is tagged at the C-terminal end of RpL3 (light blue) or RpS13 (light green), while mCherry (red) is tagged at the C-terminal end of RpL23 (dark blue) or RpS11 (light green).

(B) A simplified schematic of the SPEED, FRET, and narrow-field fluorescence microscopy setups is presented, with optical lenses on the excitation laser optical path used to convert microscopy imaging from SPEED mode to narrow-field mode. RM and DM refer to the reflection and dichroitic mirrors, respectively.

Figure 1. *Continued*

(C) A narrow-field illuminated live cell expressing FRET-pair labeled pre-ribosomal subunits (red dots) and GFP-labeled NE (green ring) is shown, with purple pseudo-colored nucleoli.

(D) A simplified diagram demonstrating the vertical single-point illumination (blue beam) of SPEED microscopy to image a single NPC in the axial and lateral planes.

(E) An illustration of a successful or abortive nuclear export event of FRET-pair labeled pre-ribosomal subunits through a GFP-labeled NPC is provided.

(F) A frame-by-frame depiction of a typical successful nuclear export event of the pre-60S subunit (red spot) through a single NPC (green spot) imaged by SPEED microscopy is displayed (Video S1).

(G) The plotted 2D trajectory of the successful event shown in F is provided.

(H) A frame-by-frame depiction of a typical abortive nuclear export event of the pre-60S subunit (red spot) through a single NPC (green spot) imaged by SPEED microscopy is displayed (Video S2).

(I) The plotted 2D trajectory of the abortive event shown in H is presented. The nucleoplasm and cytoplasm are referred to as N and C, respectively. The scale bars are 1 μm. Videos of the pre-60S (Videos S1 and S2) and pre-40S (Videos S3 and S4) nuclear export events are presented in the supplementary.

complexes. To achieve this, a fluorescent FRET-pair labeling approach was used, with two selected neighboring r-proteins labeled with GFP and mCherry. These r-proteins come into proximity once assembled into pre-ribosomal subunits and remain assembled during translation of proteins in the cytoplasm. As shown in Figure 1A, two protein pairs, rpL3-GFP/rpL23-mCherry and rpS13-GFP/rpS11-mCherry, were chosen to label pre-60S and pre-40S particles, respectively. The distance between each paired protein is less than the Förster distance of GFP and mCherry (~5.2 nm) when in proximity, indicating more than 50% energy transfer between donor and acceptor. The r-proteins rpS13 and rpS11 were specifically chosen for pre-40S particles as they have been shown to co-precipitate with pre-40S RNA more than any other measured 40S proteins and are considered essential to subunit formation.[45–47] Similarly, large-subunit proteins L3 and L23 are loaded onto the forming large ribosomal particle at two different intermediate stages of assembly prior to nuclear export through the NPCs.[46] To avoid tracking lone r-proteins or contaminated protein complexes, r-proteins were carefully selected based on their moonlight functions, and rpL23 and rpS19 were selected as their described moonlight functions are in the nucleus and nucleolus.[48] C-terminus tags were used for all the chosen r-proteins as N-terminus tagged r-proteins showed abnormal distribution upon expression in living cells.[49] Epifluorescence imaging in live cells showed that the FRET pair r-proteins are retained within each pre-ribosomal subunit from complex formation in the nucleolus to complex maturation in the cytoplasm (Figures 1B and 1C). This design to track nuclear export of assembled pre-ribosomal subunits is further validated by the completely different transport kinetics obtained for lone-labeled r-proteins examined in this study.

Prior to single-molecule tracking experiments, we also analyzed protein-protein interactions involving pre-ribosomal r-proteins, accessory proteins, and NTRs using a Search Tool for the Retrieval of Interacting Genes/Proteins (STRING) analysis[50] (Figures S1 and S2, **Additional Methods in Suppl. Info.**). The analysis revealed the association of various proteins with pre-60S and pre-40S subunits and allowed us to identify proteins containing an NES using NES prediction software. After applying filters, we identified 7 and 8 potential NESs in the pre-60S and pre-40S ribosomal subunits, respectively. Specifically, pre-60S subunits contained NES-positive ribosomal proteins such as rpL3, rpL30, and rpL35, as well as accessory proteins including eIF6, TMA16, LLPH, and NMD3. For pre-40S subunits, the NES-positive ribosomal proteins were rpS3A, rpS6, rpS16, rpS17, and rpS19, while the NES-positive accessory proteins were BYSL, TSR1, and LTV1 (Figures S3A and S3B, Table S1).

Visualizing single intact pre-ribosomal subunits undergoing nuclear export using high-speed single-molecule microscopy

We were able to localize individual NPCs at the NE of live HeLa cells by using cells that stably express POM121-GFP, a structural nucleoporin (NUP) located at the central scaffold of the NPC. We used the SPEED microscopy vertical illumination setup to capture the location of POM121-GFP with an exposure time of 1–3 s, achieving a spatial localization precision of <3nm (Figure 1D).[19,20] To prevent potential interference from POM121-GFP as a donor in FRET measurements, we photobleached the fluorescence of POM121-GFP immediately before detecting smFRET signals in our experiments. This photobleaching also reduced background noise, enabling the subsequent single particle tracking of pre-60S or pre-40S particles as they pass through the native NPC.

We tracked smFRET signals using low expression levels of the acceptor in the FRET pair (rpL23-mCherry or rpS11-mCherry) while particles interacted with a single NPC (Figure 1E). After tracking the particle

trajectories through the NPC, we analyzed and categorized them into three distinct groups: successful, abortive, and incomplete events. A successful event is when a particle transits from the nucleoplasm through the NPC to the cytoplasm (Figures 1F and 1G). An abortive event is when a particle enters the NPC from the nucleoplasm but then returns to the nucleoplasm (Figures 1H and 1I). Incomplete events occur when the trace starts in the nucleoplasm but does not extend into the cytoplasm or return to the nucleoplasm. We discard incomplete events and exclude them from the final analysis. We determine the export efficiency by dividing the number of successful export events by the total number of successful and abortive events. Additionally, we obtained the transport time of pre-ribosomal particles through the NPC by determining the dwelling times within the NPC, which provided a mean export time for the complex under investigation.

Transport efficiencies of pre-60S or pre-40S particle through NPCs in live cells

To ensure sufficient statistical power, we collected and analyzed hundreds of single-molecule traces. For the pre-60S particles, we obtained 369 single-molecule export events from eight discrete NPCs in eight different cells, of which 67 $\pm$ 3% were classified as successful (Figures 2A and S4). For the pre-40S, we recorded 261 export events from eight discrete NPCs in eight separate cells, of which 64 $\pm$ 3% were classified as successful (Figures 2C and S4). Both pre-60S and pre-40S particles showed peak locations at the center of the NPC, approximately 2 nm from the NPC center labeled by POM121-GFP (Figures 2A and 2C). Notably, the last interaction before successfully exiting the NPC occurred primarily in the cytoplasmic region of the NPC (20 nm–70 nm on the x axis) and to a lesser extent in the central scaffold region (−20 nm–20 nm on the x axis) for both particles (Figures 2B and 2D). However, most of the abortive export traces for both pre-60S and pre-40S were concentrated at the nuclear basket region of the NPC (−100 nm–−20 nm in the x-dimension), with only a small portion extending into the central scaffold region (−20 nm–20 nm on the x axis) but not beyond. The deepest penetration analyses of abortive events for both pre-60S (Figures 2E and 2F) and pre-40S (Figures 2G and 2H) confirmed that the central scaffold region of the NPC was the furthest distance they could explore. These findings suggest that both pre-60S and pre-40S particles have a higher probability of completing their nuclear export once they traverse the NPC's nuclear basket and center to reach the cytoplasmic side of the pore, where dissociation into the cytoplasm is to occur.

Furthermore, we assessed the nuclear export efficiency and time for RpL23-mCherry, RpS19-GFP, and GFP-CRM1 in live cells using single-molecule microscopy (Figures 2L and 3, Table S2). While it is possible that these two ribosomal proteins may be traveling alone or in complexes, and CRM1 may be moving with or without cargos in live cells, all three molecules exhibited a nuclear export efficiency of approximately 50%, which is consistent with the previously reported times for NTRs or facilitated transport.[19,20,52] However, this efficiency is significantly lower than the nuclear export efficiency observed for both pre-ribosomal subunits. Furthermore, when compared to other large cargos such as mRNA with a nuclear export efficiency of approximately 36% and adeno-associated viral particles with a nuclear import efficiency of about 17%,[21,53] pre-ribosomal subunits demonstrate a much higher efficiency in traversing the NPCs. These findings collectively suggest that these large pre-ribosomal particles may employ a distinct transport mechanism.

Finally, we were also interested to explore whether large pre-ribosomal particles occupy the entire central channel of the NPC during transport, given their comparable size. Our analysis of 2D probability density maps of successful nuclear export trajectories showed that both pre-ribosomal particles were concentrated along the central nucleocytoplasmic transport axis and appeared to occupy a large portion of the channel (Figures 2J and 2K). However, their occupancy pattern in the NPC differed from the passive diffusion route taken by small molecules like free GFPs, although there was some overlap[20] (Figure 2I). To further distinguish between these routes, live-cell trafficking studies using 3D super-resolution microscopy imaging will be required.

Transport time of pre-60S and pre-40S particles through the NPC in live cells

We used single-molecule traces of pre-ribosomal particles to determine the successful nuclear export time and the dwelling time for abortive events for both pre-ribosomal subunits (Figures 1G, 1I, and 3A–3D). As shown in Figures 3A and 3C, the successful nuclear export time was found to be 13 $\pm$ 1 ms and 9 $\pm$ 1 ms for pre-60S and pre-40S, respectively (Figures 3A and 3C). The smaller size and more exposed NESs of pre-40S may account for its shorter nuclear export time (Figures 4A and 4B, Table S2). Similarly, the dwell time for abortive export events of pre-40S particles is shorter than that of pre-60S, although the difference is smaller

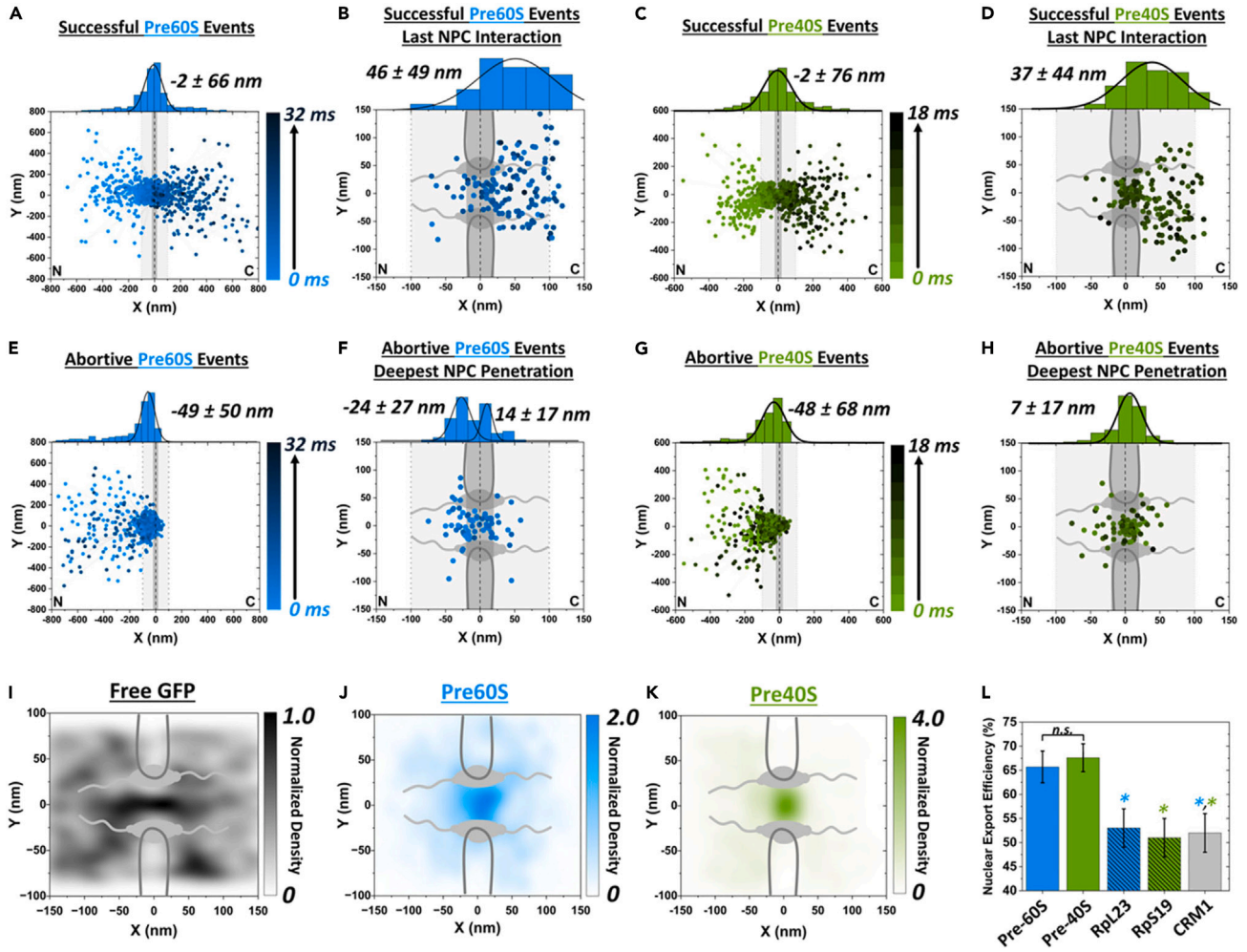

Figure 2. Single-molecule trajectories, probability density maps, and successful export efficiency of pre-ribosomal particles through the NPCs

(A) Superimposed single-molecule trajectories from 138 successful transport events for pre-60s. Each event is color-coded ranging from 0 ms to 32 ms, with 32 ms being the longest event. Histogram of successful events for pre-60s by the X (nm) dimension, fitted by a Gaussian function yielding a peak position at −2 ± 66 nm on the nuclear side of the NPC.

(B) Last recorded step of the successful events for pre-60s particles before exiting the NPC superimposed over an NPC illustration (gray), with a histogram of X (nm) data yielding a peak position at 46 ± 49 nm.

(C) Single-molecule trajectories from 173 successful transport events for pre-40s. Each event is color-coded ranging from 0 ms to 18 ms, with 18 ms being the longest event. Histogram of successful events for pre-40s by the X (nm) dimension with a peak position at −2 ± 76 nm on the cytoplasmic side of the NPC.

(D) Last recorded step of the successful events for pre-40s particles before exiting the NPC, with an X (nm) peak position of 37 ± 44 nm.

(E) Single-molecule trajectories from 72 abortive events for pre-60s with an X (nm) peak position of −49 ± 50 nm.

(F) Deepest penetration into the NPC from the recorded abortive events in E, with X (nm) peak positions at −24 ± 27 nm and 14 ± 17 nm.

(G) Single-molecule trajectories from 83 abortive events for pre-40s with an X (nm) peak position of −48 ± 68 nm.

(H) Deepest penetration into the NPC from the recorded abortive events in G, with a peak position of 7 ± 17 nm.

(I) Freely diffusing GFP 2D probability density map of successful and abortive events from previously published research article,[20] used with permission. Normalized to the background.

(J) Pre-60S 2D probability density map of successful and abortive events from A and E, normalized to the freely diffusing GFP shown in I.

(K) Pre-40S 2D probability density map of successful and abortive events from C and G, normalized to the freely diffusing GFP shown in I.

(L) Nuclear export efficiency of intact pre-60S (blue), intact pre-40S (green), single pre-60S associated r-protein, rpL23 (blue with black lines), single pre-60S associated r-protein, rpS19 (green with black lines), and associated NTR CRM1 (gray) live cell nuclear export efficiency. The dotted black line indicates the 0 nm position in the X-dimension and the center of the NPC. The dark gray shaded region outlines the −20 nm–20 nm position and outlines the approximate distance of the central scaffold region. The light gray shaded region indicates the −100 nm to −20 nm and 20 nm–100 nm region of the NPC. N, nucleoplasm. C, cytoplasm. p values were calculated by two-sided Welch's t test for comparison with pre-ribosomal subunits. $p < 0.05$, *.

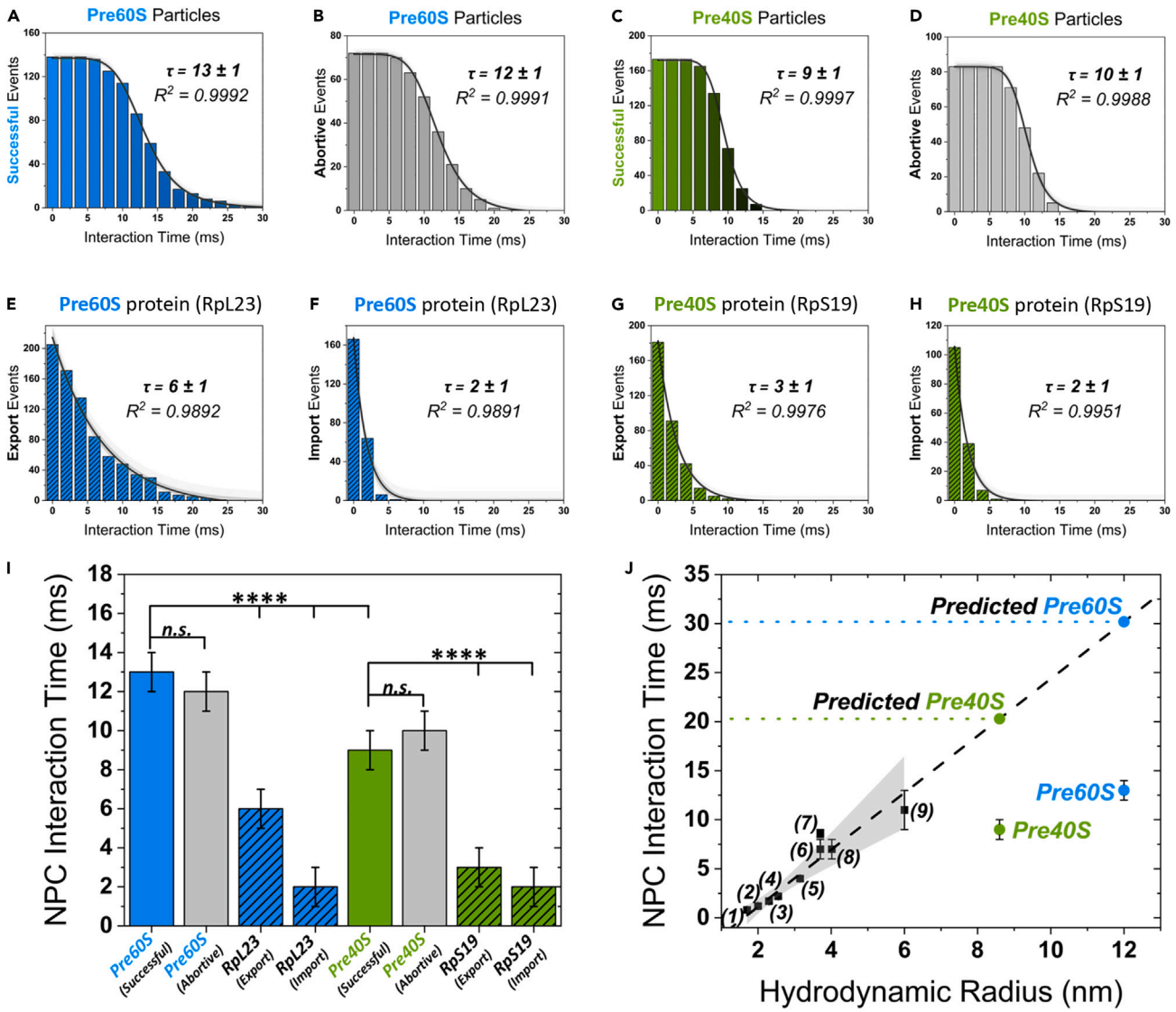

Figure 3. Nuclear transport time for pre-ribosomal particles and ribosomal proteins

(A) Nuclear export time distributions for successfully transported pre-60S particles fitted by a Hill function, with a transport time of 13 ± 1 ms.

(B) Nuclear export time distributions for abortive pre-60S transport events, fitted by a Hill function with a transport time of 12 ± 1 ms.

(C) Successful and (D) abortive nuclear export time distributions for pre-40S particles with transport times of 9 ± 1 ms and 10 ± 1 ms, respectively, fitted by Hill functions.

(E) Nuclear export time distribution for single pre-60S r-protein, rpL23, fitted by an exponential decay function, with a transport time of 6 ± 1 ms.

(F) Nuclear import time distribution for all rpL23 import events fitted by an exponential decay function, with a transport time of 2 ± 1 ms.

(G) Nuclear transport time distributions for single pre-40S r-protein, rpS19, export (G) and import (H) events with transport times 3 ± 1 ms and 2 ± 1 ms, respectively, fitted by an exponential decay function.

(I) Nuclear transport times for successful export events of pre-60S (blue), successful export events of pre-40S (green), abortive events of pre-60S (gray), abortive events pre-40S (gray), export and import events of RpL23 (blue with black lines) and export and import events of RpS19 (green with black lines).

(J) Nuclear transport times of previously published molecules[20,21]: (1) Alexa Fluor (AF) 488 labeled 3-kDa Dextran, (2) AF647 labeled insulin, (3) AF647 labeled 10-kDa Dextran, (4) AF647 labeled α-lactalbumin, (5) AF647 labeled GFP, (6) AF647 labeled cargo complexes of IBB-2xMBP-M3/Impβ1, (7) AF647 labeled cargo complexes of NLS-2xGFP/Impα/Impβ1, (8) AF647 labeled complexes of IBB-2xMBP-M3/Impβ2, and (9) mCherry labeled mRNP. Error bars indicate the *SE* for nuclear transport times. The hydrodynamic radius was calculated using the Stokes radius formula.[51] Panels A–D nuclear export time distributions best fit to a Hill function. Panels E–H nuclear transport time distributions best fit to an exponential decay function. P-values were calculated by two-sided Welch's t test for comparison with pre-ribosomal subunits. Not significant, *n.s.*, $p < 0.0001$, ****. The shaded gray region shown in J represents a 95% confidence interval. The black dotted line is a projection of the best line fit for the black data points.

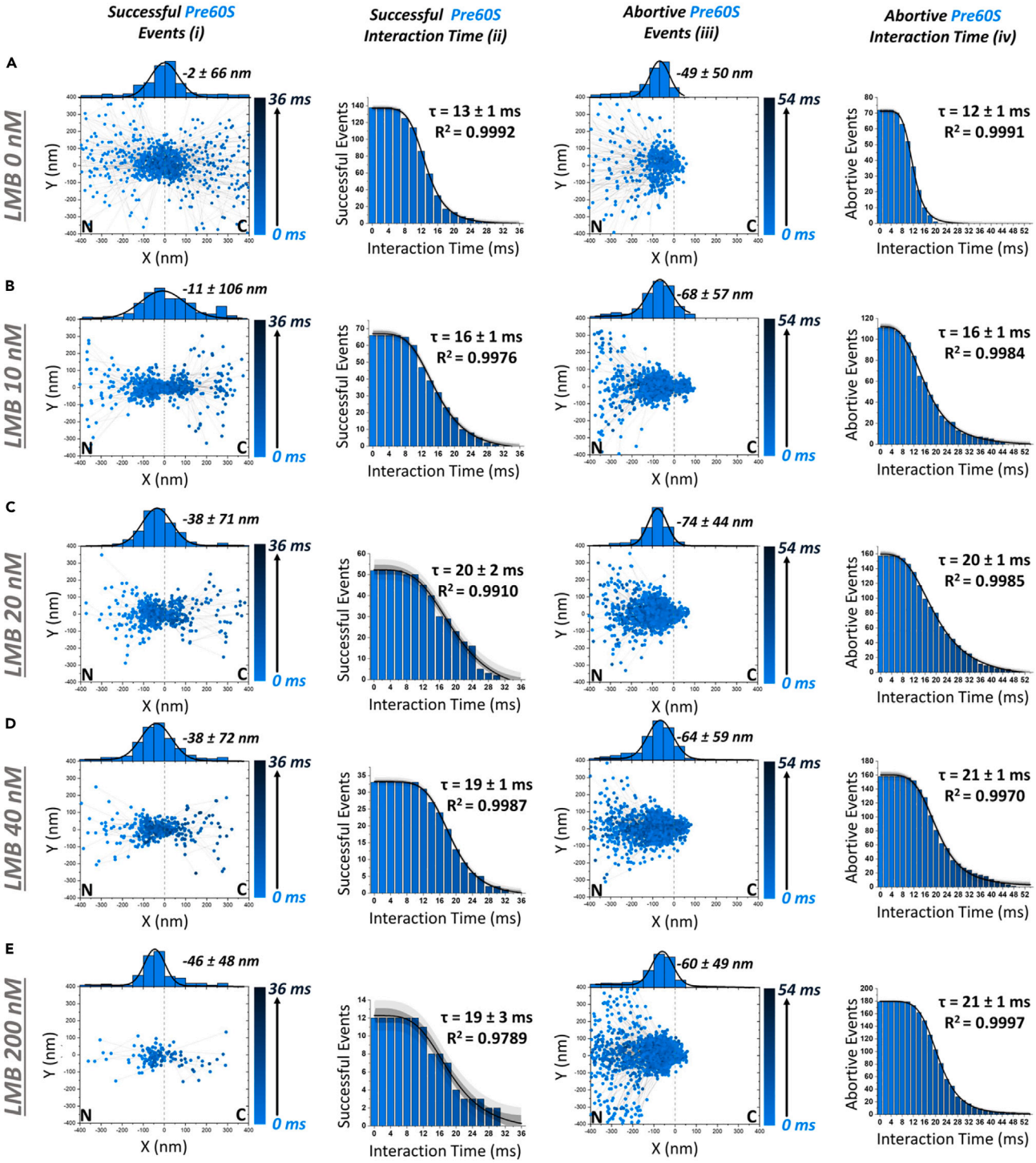

Figure 4. Effect of LMB on single-molecule trajectories and nuclear export kinetics of pre-60S through single NPCs

(A–E) Single-molecule trajectories and nuclear export time of pre-60S through single NPCs were quantified at various LMB concentrations: (A) 0 nM, (B) 10 nM, (C) 20 nM, (D) 40 nM, and (E) 200 nM. Successful (i-ii) and abortive (iii-iv) nuclear export events were demonstrated separately, and each event was color-coded ranging from 0 ms to its longest time in ms. A frequency count histogram of successful or abortive events in relation to interaction time (ms) within the NPC was fit with a Hill equation, generating the time constant (τ) and R2 value. The fitting line is shown in red and the dark gray region indicates a 95% confidence interval, while the light gray region indicates a 95% prediction interval.

(Figures 3B and 3D). The export time observed for pre-ribosomal particles through the NPCs is 2–6 times longer than the nuclear import and export time measured for r-proteins RpL23 and RpS19 in live cells (Figures 3E–3H). It is noteworthy that, for both r-proteins, their nuclear export time is always longer than their nuclear import time, which may suggest that they import alone but export by chance to associate with complexes.

The exponential decay function was a good fit for the nuclear transport time of r-proteins (Figure 3E–3H). However, the dwell times of pre-60S and pre-40S particles within the NPCs were not well described by the commonly used exponential decay function in nucleocytoplasmic transport studies.[53–63] Instead, these dwell times were better described by either a Hill function or an inverse sigmoidal function, both of which yielded almost identical export times (Figures 3A–3D). In this study, we ultimately used the Hill function to obtain export times for pre-ribosomal subunits. In contrast to exponential decay, an inverse sigmoidal function typically has a plateau at the initial stage prior to the start of decay. Additionally, a Hill function is useful in capturing biomolecular interactions that exhibit cooperativity between two binding molecules. These findings may suggest that pre-ribosomal subunits, being large particles that have multiple NESs requiring multiple NTRs, have a distinct transition model different from protein cargos typically bearing single NES, and support the existence of two likely states of transport, including initial docking at and transporting through the NPC.

Remarkably, we observed a significant deviation from the best fit trendline when comparing the nuclear transport times of pre-60S and pre-40S particles to those of passively transiting and facilitated cargo molecules in previous studies.[37] Based on their hydrodynamic radius,[51] pre-60S and pre-40S were predicted to have transport time of ~30 ms and ~20 ms, respectively, which were almost two times longer than the export time that we observed (Figure 3J). The export time fitted by Hill function that is shorter than anticipated, together with the high export efficiency, further supports the possibility that pre-ribosomal particles likely have a unique mode of transport that involves multiple NTRs working cooperatively.

Nuclear export of pre-ribosomal particles inhibited by Leptomycin B

Potential NESs have been identified in the pre-60S and pre-40S subunits (Figures S3A and S3B, Table S1), with seven and eight sites respectively, which can be recognized by multiple CRM1 to enhance nuclear export. To inhibit CRM1 activity, we used Leptomycin B (LMB), a CRM1 inhibitor, and designed experiments to study the effect of LMB on pre-ribosomal particles. Live cells were firstly incubated with titrated concentrations of LMB (0 nM–200 nM), and any changes in the subcellular localization of FRET-pair-labeled pre-ribosomal particles were examined in fixed cells. Employing the epifluorescence mode of the SPEED microscopy setup, we compared the spatial distributions of labeled pre-ribosomal subunits under different concentrations of LMB (0 nM, 10 nM, 20 nM, 40 nM, and 200 nM). By analyzing the fluorescence intensity differences between the nucleus and cytoplasm in 50–60 cells for both pre-60S and pre-40S, we plotted the intensity ratio and found that more pre-ribosomal particles were restricted in the nucleus as the concentration of LMB increased from 0 nM to 40 nM, with a trend reaching saturation at 200 nM (Figures S3C–S3F).

Next, we further quantified the nuclear export time and efficiency of pre-ribosomal subunits in live cells under the LMB treatments at the single-molecule level (Figures 4, 5, and 6). The results showed that LMB treatment led to a drastic reduction in nuclear export efficiency and a significant increase in nuclear export time for both pre-60S and pre-40S particles. Specifically, for pre-60S, the nuclear export efficiency was 66 $\pm$ 3%, 37 $\pm$ 4%, 25 $\pm$ 3%, 17 $\pm$ 3%, and 6 $\pm$ 2% at LMB concentrations of 0 nM, 10 nM, 20 nM, 40 nM, and 200 nM, respectively (Figure 6A, Table S2). The nuclear export time was 13 $\pm$ 1ms, 16 $\pm$ 1ms, 20 $\pm$ 2ms, 19 $\pm$ 1ms, and 19 $\pm$ 3ms, respectively (Figures 4, 6B, and 6C, Table S2). Similarly, for pre-40S, the nuclear export efficiency was 68 $\pm$ 3%, 38 $\pm$ 4%, 23 $\pm$ 3%, 15 $\pm$ 3%, and 4 $\pm$ 2%, and the nuclear export time was 9 $\pm$ 1ms, 11 $\pm$ 1ms, 14 $\pm$ 2ms, 17 $\pm$ 2ms, and 19 $\pm$ 2 ms at LMB concentrations of 0 nM, 10 nM, 20 nM, 40 nM, and 200 nM, respectively (Figures 5 and 6A–6C; Table S2).

The nuclear export efficiency of both pre-ribosomal subunits decreased significantly in a dose-dependent manner, with an approximately 11-fold decrease for pre-60S and a 17-fold decrease for pre-40S as LMB concentration increased from 0 nM to 200 nM (Figure 6A; Table S2). Single-molecule trajectories of abortive export events confirmed these results, showing an increasing number of export events blocked at the nuclear basket of the NPC before entering the central scaffold region as more LMB was added (Figures 4-iii

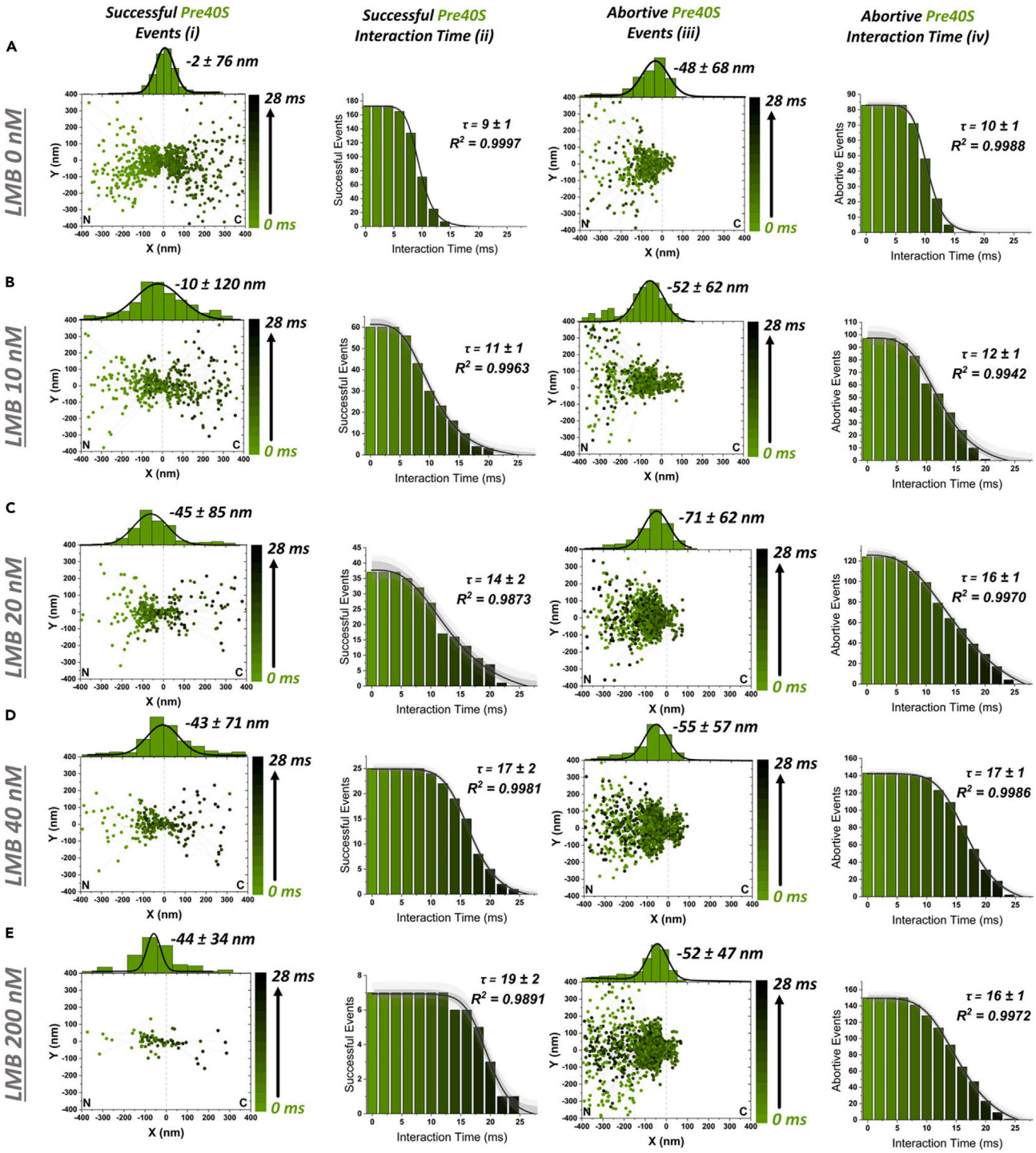

Figure 5. Effect of LMB on single-molecule trajectories and nuclear export kinetics of pre-40S through single NPCs

(A–E) Single-molecule trajectories and nuclear export time of pre-40S through single NPCs were quantified at various LMB concentrations: (A) 0 nM, (B) 10 nM, (C) 20 nM, (D) 40 nM, and (E) 200 nM. Successful (i-ii) and abortive (iii-iv) nuclear export events were demonstrated separately, and each event was color-coded ranging from 0 ms to its longest time in ms. A frequency count histogram of successful or abortive events in relation to interaction time (ms) within the NPC was fit with a Hill equation, generating the time constant (τ) and R2 value. The fitting line is shown in red and the dark gray region indicates a 95% confidence interval, while the light gray region indicates a 95% prediction interval.

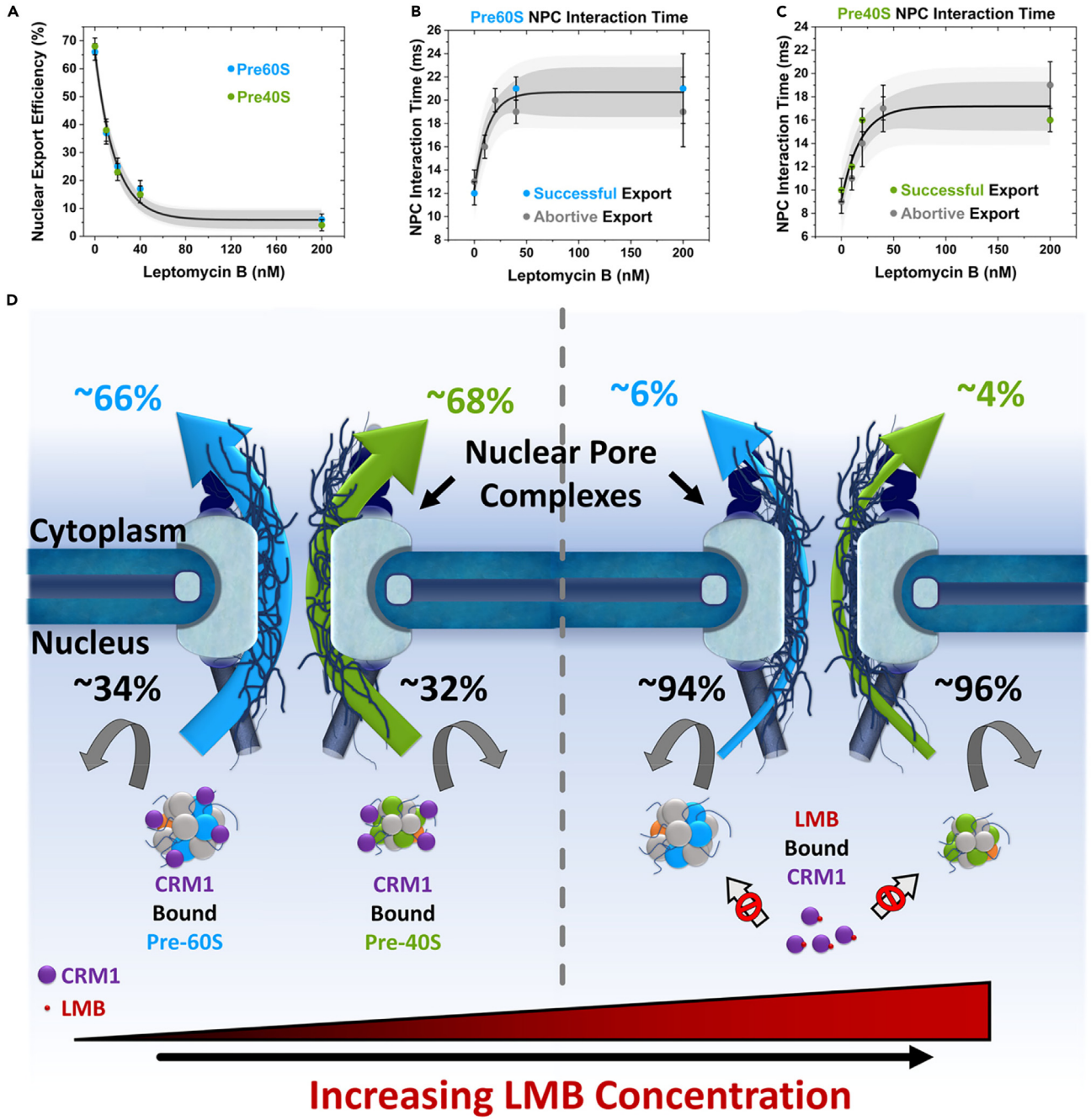

Figure 6. Summary of LMB effects on nuclear export kinetics for pre-ribosomal particles and a proposed model for their efficient nuclear export

(A) Nuclear export efficiency of pre-60S and pre-40S under LMB treatment, shown as an exponential decay function best fit to the data (solid black line).

(B) Successful (blue) and abortive (gray) nuclear transport times for pre-60S under LMB treatment, shown as a natural log function best fit to the data (solid black line).

(C) Successful (green) and abortive (gray) nuclear transport times for pre-40S under LMB treatment, shown as a natural log function best fit to the data (solid black line).

(D) Proposed model for CRM1-mediated nuclear export of pre-ribosomal particles without (left panel) and with (right panel) LMB treatment. The dark and light shaded gray regions shown in A–C represent a 95% confidence interval and 95% prediction interval, respectively.

and 5-iii). Interestingly, single-molecule trajectories of successful export events revealed that the spatial location of the interaction sites between pre-ribosomal particles and the NPC shifted away from the center of the NPC scaffold toward the nuclear basket as LMB consumed more CRM1 at higher concentrations

(Figures 4-i and 5-i). This shift indicates that abundant CRM1 is required to assist large pre-ribosomal particles in traversing the NPC's nuclear basket and center to reach the cytoplasmic side of the pore before being released into the cytoplasm.

While the export efficiency decreased precipitously, the export time only increased by approximately 50% as LMB concentration increased from 0 nM to 40 nM and remained unchanged until 200 nM for both subunits. These findings suggest that LMB-induced inadequate CRM1 has a more severe impact on nuclear export efficiency than nuclear export time for pre-ribosomal particles. Inadequate CRM1 may cause longer initial docking times for large cargo at the nuclear basket, but subsequent transport or diffusion time through the center and cytoplasmic side of the NPC were less affected. However, the lack of CRM1 can compromise interactions between CRM1 and FG Nups throughout the NPC, leading to significantly reduced nuclear export efficiency.

Enhancement of nuclear transport efficiency for protein cargos by multiple NTRs: *In vitro* and *in vivo* examples

Our investigations propose a model for the nuclear export of pre-60S and pre-40S subunits, in which multiple copies of CRM1 function cooperatively to chaperone pre-ribosomal subunits through the NPC, leading to increased export efficiency and decreased export time. Previous studies have also shown that multivalent binding of NTRs can enhance nuclear transport of protein cargos or viral particles that bear multiple nuclear localization sequences (NLSs) or NESs.[64–66] For instance, the use of a maltose-binding protein (MBP) dimer (IBB-2xMBP-M3) as the cargo protein, containing both an IBB domain and an M3 domain, has demonstrated that the simultaneous binding of IBB-2xMBP-M3 to two different NTRs can result in more efficient import.[52] Specifically, Importin β1 (Imp β1) binds to the IBB domain and Impβ2 binds to the M9 domain in M3. In contrast, binding to only one NTR does not enhance import efficiency. To quantify this observation, we used high-speed single-molecule SPEED microscopy to determine the nuclear import efficiency and time for IBB-2xMBP-M3 binding to one or two different NTRs in permeabilized cells. Noteworthy, permeabilized cells are a valuable tool for studying intracellular processes in a controlled environment, providing insights that cannot be obtained using intact cells.

To ensure that >99% of the cargo formed complexes with Impβ1, Impβ2, or both at any given time in permeabilized cell systems, we oversaturated the NTR concentration (STAR Methods). The transport kinetics of the IBB-2xMBP-M3 cargo were quantified with the addition of Impβ1, Impβ2, or a combination of both NTRs. We observed no significant difference between nuclear import efficiencies obtained for IBB-2xMBP-M3 in the presence of lone Impβ1 or Impβ2, at 52 $\pm$ 3% and 48 $\pm$ 3%, respectively. However, the nuclear import efficiency for the protein cargo in the presence of both NTRs was significantly enhanced to 65 $\pm$ 3% (Figure S5 and Table S1). Additionally, the nuclear import time for IBB-2xMBP-M3 decreased by ~30% in the presence of both NTRs. These quantitative results support the model that multiple NTRs can work cooperatively to improve nuclear transport rate.

We further bolster these findings with an example of nucleocytoplasmic transport of Smad proteins in live cells, both in the presence and absence of transforming growth factor β1 (TGF-β1).[54] Receptor-regulated Smad proteins (R-Smads), such as Smad2, and the common signaling transducer Smad protein, Smad4, can form hetero-complexes and transport through NPCs to accumulate in the nucleus under the stimulation of TGF-β. Without ligand stimulation, Smad2 or Smad4 proteins are predominantly present in the cytoplasm. To facilitate their nuclear import or export, Smad2 contains one NLS, two NESs, and a hydrophobic corridor domain that interacts with FG Nups. Smad4, on the other hand, contains one bipartite NLS recognized by Importin 7 and Importin 8, and one NES recognized by CRM1. Upon TGF-β1 stimulation, a heterotrimer comprising two Smad2 proteins and one Smad4 protein is formed in the cytoplasm, which is equipped with two NLSs, one bipartite NLS, and two hydrophobic corridor domains to facilitate nuclear import. However, all NESs are concealed within the cytoplasm, and none are exposed on the surface of the heterotrimer. Upon reaching the nucleus, the heterotrimer dissociates into individual monomers, each of which performs nuclear export independently using the export signals they carry.

By employing high-speed single-molecule SPEED microscopy and FRET techniques (STAR Methods), we monitored the complete process of TGF-β1-induced Smad2/Smad4 heterocomplex formation and dissociation, as well as their nuclear transport efficiency through NPCs in live cells.[54] Our experiments revealed that the formation of Smad2/Smad4 heterocomplexes equipped with multiple importing signals

recognized by more NTRs resulted in a nuclear import efficiency of 43 ± 3%, which is 2-fold higher than the 26 ± 4% and 22 ± 5% observed for Smad2 and Smad4 monomers, respectively. Subsequently, we found that Smad2 and Smad4 monomers equipped with one or two NESs recognized by CRM1 possessed a nuclear export efficiency of 42 ± 4% and 47 ± 5%, respectively, which is approximately four times higher than the low nuclear export efficiency of 12 ± 2% for their heterotrimers containing concealed NES due to conformational changes (Figure S5 and Table S2). Our observations suggest that multiple NTRs can enhance the import or export efficiency of endogenous protein cargoes in live cells.

DISCUSSION

In this study, we utilized high-speed single-molecule tracking microscopy combined with FRET techniques to investigate the transport dynamics of individual intact pre-ribosomal subunits through NPCs in live cells. Our results provide strong evidence that pre-60S and pre-40S particles exit the nucleus with high export efficiencies exceeding 65%, and with export times that are significantly lower than anticipated based on their hydrodynamic radius alone. We have shown that the association of multiple CRM1s enhances the efficient nuclear export for these pre-ribosomal particles, which is supported by computational analysis of both r-proteins and accessory proteins, experimental observations from LMB drug inhibition, and 2D single-molecule trajectories of export events. These findings provide significant support for a model of nuclear export through the NPC for pre-ribosomal subunits, where pre-60S and pre-40S achieve superior export efficiency and decreased export time due to the involvement of multiple CRM1s. Interestingly, this mechanism may not be restricted solely to large cargoes, such as pre-ribosomal particles. Indeed, nucleocytoplasmic transport assays conducted on both permeabilized and live cells suggest that the involvement of multiple NTRs in nuclear import or export can enhance the efficiency of protein transport as well.

The administration of LMB, a drug that blocks the binding of CRM1 to NES-carrying cargo, had a significant impact on the nuclear export rate of both pre-ribosomal subunits in a dose-dependent manner. The export time for both pre-ribosomal subunits was prolonged by roughly 50%, and the export efficiency was reduced by 11-fold to around 6% for pre-60S and 17-fold to approximately 4% for pre-40S at high LMB concentrations. These findings suggest that of the NTRs, including CRM1, TAP-p15, and the export adaptor Rrp12 for pre-60S, and CRM1 and Rrp12 for pre-40S,[27,28,30–34,67,68] CRM1 plays a significant role in driving efficient nuclear export for pre-ribosomal subunits. While TAP-p15 and Rrp12 have been suggested to play a role in the export of these pre-ribosomal subunits, there is limited direct evidence that clearly outlines their individual functions in the export of these subunits. This is primarily due to the necessity of these transport receptors in cellular viability, as attempts to knock them out resulted in cell death (Figure S6), making it challenging to evaluate their specific contributions.[28,69,70] However, accumulating evidence strongly implicates that CRM1 is the primary driver of nuclear export for pre-60S and pre-40S.

Even though nearly two-thirds of pre-ribosomal particles interacting with NPCs are successfully exported through the NPC and into the cytoplasm, one-third of them are returned to the nucleoplasm. Through a comparison of 2D single-molecule localizations of successful and abortive nuclear export events for pre-ribosomal subunits, it was discovered that these subunits have a high likelihood of completing their nuclear export once they traverse two critical subregions of the NPC, namely the nuclear basket and the NPC center. Failing to pass through these regions results in abortive events, and these regions appear to function as selectivity barriers for pre-ribosomal particles within the NPC. It is noteworthy that recent studies have indicated that the nuclear transport of protein complexes facilitated by a single NTR is mainly restricted by the NPC central region rather than the nuclear basket and center,[19,20] implying that very large cargos such as pre-ribosomal subunits may have somewhat different transport mechanisms. Within the context of this model for pre-ribosomal subunits, we can infer that as the concentration of CRM1 is depleted under LMB treatments, the pre-ribosomal particle initially docks within the nuclear basket, where it either recruits additional CRM1 to continue exporting through the NPC or fails to do so and returns to the nucleoplasm.

The transport of pre-ribosomal particles through the NPC has been extensively studied in yeast cells, providing significant insights into this process in these organisms.[5,6,30,31,33,34,36,37] However, relatively few studies have examined pre-ribosomal particles in metazoan cells, with one notable exception. Recently, Ruland et al. evaluated the transport kinetics of pre-60S particles in mammalian cells using a combination of biochemical data and narrow-field HiLo microscopy.[38] Remarkably, the transport times reported by Ruland et al. largely agree with those reported in this study. However, the functional forms of

the curves that fit the transport times differ. While Ruland et al.'s data could be fit by an exponential decay function, the transport times reported in this study are better described by a Hill or sigmoidal function, suggesting distinct docking and exporting steps. This difference can be partially attributed to the temporal resolution at imaging, with Ruland et al. using an imaging speed of 14 ms and this study using a faster 2 ms imaging speed.

In addition, Ruland et al. reported that approximately one-third of pre-60S and NPC interactions resulted in a successful export, while this study achieved a higher export efficiency by using an FRET-based labeling strategy for pre-60S and pre-40S. The difference in export efficiency can be likely explained by different labeling strategies used in the studies. This study observed single-molecule isolation and identification by using the inherent properties of FRET to temporally and spatially separate and localize FRET-pair-labeled pre-ribosomal subunits, ensuring that only assembled pre-ribosomal subunits were tracked. Notably, this study is also the first to characterize pre-40S nuclear export dynamics at the single-molecule level in mammalian cells. Despite the disagreement between the two studies, the agreement in export efficiency between pre-40S and pre-60S within this study and between this study and Ruland et al. regarding export time suggests that these data are reliable and consistent.

Future directions for this project will include mutational studies on identified NES of selected candidate r-proteins/accessory proteins to further solidify the conclusion that the transport of pre-ribosomal subunits is aided by multiple NTR binding. This will involve building protein binding assays with mutated NES, which will serve as an asset for the scientific community. Since Exportin 5 has been identified as having an essential role in pre-60S export,[64] we are also interested in expanding our research to discretely evaluate the roles of other export receptors, including Exportin 5. In addition to pre-ribosomal particles, the NPC has been shown to be capable of transporting other large cargoes (>15 nm), such as viral capsids, proteasome components, and synthetic vectors for drug or gene therapy delivery.[65,66,71] Therefore, we are interested in expanding this study to quantify nucleocytoplasmic kinetics for these large particles in various cell systems. This will provide valuable insights into the general mechanisms of nuclear transport and could potentially have significant implications for drug and gene therapy development.

Limitations of the study

In this study, the primary use of smFRET signal is to spatially and temporally separate and localize FRET-pair-labeled pre-ribosomal subunits, ensuring the tracking of assembled pre-ribosomal subunits during nuclear export in live cells. However, it is important to acknowledge the inherent capabilities of smFRET that make it a powerful tool for investigating biomolecular interactions, dynamics, and conformational changes with exceptional sensitivity and single-molecule resolution. While our current manuscript does not fully exploit these advantages of smFRET to explore potential conformational changes in the large pre-ribosomal subunits during their nuclear export, we acknowledge the significant potential for further investigation. To accurately determine such changes, our future plans involve enhancing our microscopy imaging techniques to reduce background noise, minimize fluorophore photobleaching, and differentiate between genuine conformational changes and photophysical artifacts. Additionally, we intend to explore the potential of utilizing the virtual three-dimensional (3D) imaging capabilities offered by SPEED microscopy.[19–22] The implementation of 3D imaging will allow us to address unresolved questions concerning the spatial occupancy of large cargos within the sub-micrometer NPC during the nuclear export of pre-ribosomal subunits. It will also provide insights into how these large cargos navigate transport routes while coexisting with the passive diffusion of small molecules, as well as the facilitated transport of proteins and mRNAs. By leveraging the 3D imaging capabilities of SPEED microscopy and the conformational determination provided by smFRET, we anticipate unraveling the more intricate dynamics of nucleocytoplasmic transport and shedding light on the interplay between different molecular species within the NPC.

STAR★METHODS

Detailed methods are provided in the online version of this paper and include the following:

- KEY RESOURCES TABLE
- RESOURCE AVAILABILITY
  - Lead contact
  - Material availability
  - Data and code availability

SUPPLEMENTAL INFORMATION

Supplemental information can be found online at https://doi.org/10.1016/j.isci.2023.107445.

ACKNOWLEDGMENTS

The project was supported by grants from the US National Institutes of Health (NIH GM097037, GM116204, and GM122552 to W.Y.).

AUTHOR CONTRIBUTIONS

W. Y. designed experiments. S. L. J., M. T., J.M.K., and W. Y. wrote the manuscript. S. L. J., J.M.K., A.G., K. H., and W.Y. performed experiments and analyzed the data.

DECLARATION OF INTERESTS

The authors declare no competing interests.

Received: December 19, 2022
Revised: June 24, 2023
Accepted: July 18, 2023
Published: July 21, 2023

REFERENCES

1. Schäfer, T., Strauss, D., Petfalski, E., Tollervey, D., and Hurt, E. (2003). The path from nucleolar 90S to cytoplasmic 40S pre-ribosomes. EMBO J. *22*, 1370–1380. https://doi.org/10.1093/emboj/cdg121.

2. Greber, B.J. (2016). Mechanistic insight into eukaryotic 60S ribosomal subunit biogenesis by cryo-electron microscopy. RNA *22*, 1643–1662. https://doi.org/10.1261/rna.057927.116.

3. Bohnsack, K.E., and Bohnsack, M.T. (2019). Uncovering the assembly pathway of human ribosomes and its emerging links to disease. EMBO J. *38*, e100278.

4. Liang, X., Zuo, M.-Q., Zhang, Y., Li, N., Ma, C., Dong, M.-Q., and Gao, N. (2020). Structural snapshots of human pre-60S ribosomal particles before and after nuclear export. Nat. Commun. *11*, 3542. https://doi.org/10.1038/s41467-020-17237-x.

5. Anger, A.M., Armache, J.-P., Berninghausen, O., Habeck, M., Subklewe, M., Wilson, D.N., and Beckmann, R. (2013). Structures of the human and Drosophila 80S ribosome. Nature *497*, 80–85. https://doi.org/10.1038/nature12104.

6. Lo, K.-Y., and Johnson, A.W. (2009). Reengineering Ribosome Export. Mol. Biol. Cell *20*, 1545–1554. https://doi.org/10.1091/mbc.e08-10-1000.

7. Ameismeier, M., Cheng, J., Berninghausen, O., and Beckmann, R. (2018). Visualizing late states of human 40S ribosomal subunit maturation. Nature *558*, 249–253. https://doi.org/10.1038/s41586-018-0193-0.

8. Tingey, M., Li, Y., Yu, W., Young, A., and Yang, W. (2022). Spelling out the roles of individual nucleoporins in nuclear export of mRNA. Nucleus *13*, 170–193. https://doi.org/10.1080/19491034.2022.2076965.

9. Tingey, M., Mudumbi, K.C., Schirmer, E.C., and Yang, W. (2019). Casting a Wider Net: Differentiating between Inner Nuclear Envelope and Outer Nuclear Envelope Transmembrane Proteins. Int. J. Mol. Sci. *20*, 5248.

10. Fernandez-Martinez, J., and Rout, M.P. (2021). One ring to rule them all? Structural and functional diversity in the nuclear pore complex. Trends Biochem. Sci. *46*, 595–607.

11. Lin, D.H., Correia, A.R., Cai, S.W., Huber, F.M., Jette, C.A., and Hoelz, A. (2018). Structural and functional analysis of mRNA export regulation by the nuclear pore complex. Nat. Commun. *9*, 2319.

12. Suntharalingam, M., and Wente, S.R. (2003). Peering through the Pore: Nuclear Pore Complex Structure, Assembly, and Function. Dev. Cell *4*, 775–789. https://doi.org/10.1016/S1534-5807(03)00162-X.

13. Hoelz, A., Debler, E.W., and Blobel, G. (2011). The Structure of the Nuclear Pore Complex. Annu. Rev. Biochem. *80*, 613–643. https://doi.org/10.1146/annurev-biochem-060109-151030.

14. Tu, L.-C., Fu, G., Zilman, A., and Musser, S.M. (2013). Large cargo transport by nuclear pores: implications for the spatial organization of FG-nucleoporins. EMBO J. *32*, 3220–3230. https://doi.org/10.1038/emboj.2013.239.

15. Labokha, A.A., Gradmann, S., Frey, S., Hülsmann, B.B., Urlaub, H., Baldus, M., and Görlich, D. (2013). Systematic analysis of barrier-forming FG hydrogels from Xenopus nuclear pore complexes. EMBO J. *32*, 204–218. https://doi.org/10.1038/emboj.2012.302.

16. Denning, D.P., Patel, S.S., Uversky, V., Fink, A.L., and Rexach, M. (2003). Disorder in the nuclear pore complex: The FG repeat regions of nucleoporins are natively unfolded. Proc. Natl. Acad. Sci. USA *100*, 2450–2455. https://doi.org/10.1073/pnas.0437902100.

17. Wälde, S., and Kehlenbach, R.H. (2010). The Part and the Whole: functions of nucleoporins in nucleocytoplasmic transport. Trends Cell Biol. *20*, 461–469. https://doi.org/10.1016/j.tcb.2010.05.001.

18. Görlich, D., and Kutay, U. (1999). Transport between the cell nucleus and the cytoplasm. Annu. Rev. Cell Dev. Biol. *15*, 607–660.

19. Ma, J., and Yang, W. (2010). Three-dimensional distribution of transient interactions in the nuclear pore complex obtained from single-molecule snapshots. Proc. Natl. Acad. Sci. USA *107*, 7305–7310. https://doi.org/10.1073/pnas.0908269107.

20. Ma, J., Goryaynov, A., Sarma, A., and Yang, W. (2012). Self-regulated viscous channel in the nuclear pore complex. Proc. Natl. Acad. Sci. USA *109*, 7326–7331. https://doi.org/10.1073/pnas.1201724109.

21. Ma, J., Liu, Z., Michelotti, N., Pitchiaya, S., Veerapaneni, R., Androsavich, J.R., Walter, N.G., and Yang, W. (2013). High-resolution three-dimensional mapping of mRNA export through the nuclear pore. Nat. Commun. *4*, 2414. https://doi.org/10.1038/ncomms3414.

22. Ma, J., Goryaynov, A., and Yang, W. (2016). Super-resolution 3D tomography of interactions and competition in the nuclear pore complex. Nat. Struct. Mol. Biol. *23*, 239–247. https://doi.org/10.1038/nsmb.3174.

23. Yang, W. (2013). Distinct, but not completely separate spatial transport routes in the nuclear pore complex. Nucleus *4*, 166–175.

24. Fornerod, M., Ohno, M., Yoshida, M., and Mattaj, I.W. (1997). CRM1 Is an Export Receptor for Leucine-Rich Nuclear Export Signals. Cell *90*, 1051–1060. https://doi.org/10.1016/S0092-8674(00)80371-2.

25. Stade, K., Ford, C.S., Guthrie, C., and Weis, K. (1997). Exportin 1 (Crm1p) Is an Essential Nuclear Export Factor. Cell *90*, 1041–1050. https://doi.org/10.1016/S0092-8674(00)80370-0.

26. Ho, J.H., Kallstrom, G., and Johnson, A.W. (2000). Nmd3p Is a Crm1p-Dependent Adapter Protein for Nuclear Export of the Large Ribosomal Subunit. J. Cell Biol. *151*, 1057–1066. https://doi.org/10.1083/jcb.151.5.1057.

27. Strässer, K., Baßler, J., and Hurt, E. (2000). Binding of the Mex67p/Mtr2p Heterodimer to Fxfg, Glfg, and Fg Repeat Nucleoporins Is Essential for Nuclear mRNA Export. J. Cell Biol. *150*, 695–706. https://doi.org/10.1083/jcb.150.4.695.

28. Yao, W., Roser, D., Köhler, A., Bradatsch, B., Baßler, J., and Hurt, E. (2007). Nuclear Export of Ribosomal 60S Subunits by the General mRNA Export Receptor Mex67-Mtr2. Mol. Cell *26*, 51–62. https://doi.org/10.1016/j.molcel.2007.02.018.

29. Zemp, I., Wild, T., O'Donohue, M.F., Wandrey, F., Widmann, B., Gleizes, P.E., and Kutay, U. (2009). Distinct cytoplasmic maturation steps of 40S ribosomal subunit precursors require hRio2. J. Cell Biol. *185*, 1167–1180. https://doi.org/10.1083/jcb.200904048.

30. Rouquette, J., Choesmel, V., and Gleizes, P.-E. (2005). Nuclear export and cytoplasmic processing of precursors to the 40S ribosomal subunits in mammalian cells. EMBO J. *24*, 2862–2872. https://doi.org/10.1038/sj.emboj.7600752.

31. Peña, C., Hurt, E., and Panse, V.G. (2017). Eukaryotic ribosome assembly, transport and quality control. Nat. Struct. Mol. Biol. *24*, 689–699. https://doi.org/10.1038/nsmb.3454.

32. Taura, T., Krebber, H., and Silver, P.A. (1998). A member of the Ran-binding protein family, Yrb2p, is involved in nuclear protein export. Proc. Natl. Acad. Sci. USA *95*, 7427–7432. https://doi.org/10.1073/pnas.95.13.7427.

33. Thomas, F., and Kutay, U. (2003). Biogenesis and nuclear export of ribosomal subunits in higher eukaryotes depend on the CRM1 export pathway. J. Cell Sci. *116*, 2409–2419. https://doi.org/10.1242/jcs.00464.

34. Gadal, O., Strauß, D., Kessl, J., Trumpower, B., Tollervey, D., and Hurt, E. (2001). Nuclear Export of 60S Ribosomal Subunits Depends on Xpo1p and Requires a Nuclear Export Sequence-Containing Factor, Nmd3p, That Associates with the Large Subunit Protein Rpl10p. Mol. Cell Biol. *21*, 3405–3415. https://doi.org/10.1128/MCB.21.10.3405-3415.2001.

35. Maggi, L.B., Kuchenruether, M., Dadey, D.Y.A., Schwope, R.M., Grisendi, S., Townsend, R.R., Pandolfi, P.P., and Weber, J.D. (2008). Nucleophosmin Serves as a Rate-Limiting Nuclear Export Chaperone for the Mammalian Ribosome. Mol. Cell Biol. *28*, 7050–7065. https://doi.org/10.1128/MCB.01548-07.

36. Seiser, R.M., Sundberg, A.E., Wollam, B.J., Zobel-Thropp, P., Baldwin, K., Spector, M.D., and Lycan, D.E. (2006). Ltv1 Is Required for Efficient Nuclear Export of the Ribosomal Small Subunit in Saccharomyces cerevisiae. Genetics *174*, 679–691. https://doi.org/10.1534/genetics.106.062117.

37. Delavoie, F., Soldan, V., Rinaldi, D., Dauxois, J.-Y., and Gleizes, P.-E. (2019). The path of pre-ribosomes through the nuclear pore complex revealed by electron tomography. Nat. Commun. *10*, 497. https://doi.org/10.1038/s41467-019-08342-7.

38. Ruland, J.A., Krüger, A.M., Dörner, K., Bhatia, R., Wirths, S., Poetes, D., Kutay, U., Siebrasse, J.P., and Kubitscheck, U. (2021). Nuclear export of the pre-60S ribosomal subunit through single nuclear pores observed in real time. Nat. Commun. *12*, 6211. https://doi.org/10.1038/s41467-021-26323-7.

39. Jeffery, C.J. (1999). Moonlighting proteins. Trends Biochem. Sci. *24*, 8–11. https://doi.org/10.1016/S0968-0004(98)01335-8.

40. Li, Y., Aksenova, V., Tingey, M., Yu, J., Ma, P., Arnaoutov, A., Chen, S., Dasso, M., and Yang, W. (2021). Distinct roles of nuclear basket proteins in directing the passage of mRNA through the nuclear pore. Proc. Natl. Acad. Sci. USA *118*. e2015621118. https://doi.org/10.1073/pnas.2015621118.

41. Li, Y., Tingey, M., Ruba, A., and Yang, W. (2021). High-speed super-resolution imaging of rotationally symmetric structures using SPEED microscopy and 2D-to-3D transformation. Nat. Protoc. *16*, 532–560. https://doi.org/10.1038/s41596-020-00440-x.

42. Junod, S.L., Tingey, M., Rush, C., Alkurdi, A., Bajoria, K., and Yang, W. (2023). Obtaining 3D super-resolution images by utilizing rotationally symmetric structures and 2D-to-3D transformation. Comput. Struct. Biotechnol. J. *21*, 1424–1432. https://doi.org/10.1016/j.csbj.2023.02.008.

43. Luo, W., Ruba, A., Takao, D., Zweifel, L.P., Lim, R.Y.H., Verhey, K.J., and Yang, W. (2017). Axonemal Lumen Dominates Cytosolic Protein Diffusion inside the Primary Cilium. Sci. Rep. *7*, 15793. https://doi.org/10.1038/s41598-017-16103-z.

44. Li, Y., Aksenova, V., Tingey, M., Yu, J., Ma, P., Arnaoutov, A., Chen, S., Dasso, M., and Yang, W. (2021). Distinct roles of nuclear basket proteins in directing the passage of mRNA through the nuclear pore. Proc. Natl. Acad. Sci. USA *118*. e2015621118.

45. Ferreira-Cerca, S., Pöll, G., Gleizes, P.-E., Tschochner, H., and Milkereit, P. (2005). Roles of Eukaryotic Ribosomal Proteins in Maturation and Transport of Pre-18S rRNA and Ribosome Function. Mol. Cell *20*, 263–275. https://doi.org/10.1016/j.molcel.2005.09.005.

46. de la Cruz, J., Karbstein, K., and Woolford, J.L., Jr. (2015). Functions of Ribosomal Proteins in Assembly of Eukaryotic Ribosomes In Vivo. Annu. Rev. Biochem. *84*, 93–129. https://doi.org/10.1146/annurev-biochem-060614-033917.

47. O'Donohue, M.-F., Choesmel, V., Faubladier, M., Fichant, G., and Gleizes, P.-E. (2010). Functional dichotomy of ribosomal proteins during the synthesis of mammalian 40S ribosomal subunits. J. Cell Biol. *190*, 853–866. https://doi.org/10.1083/jcb.201005117.

48. Molavi, G., Samadi, N., and Hosseingholi, E.Z. (2019). The roles of moonlight ribosomal proteins in the development of human cancers. J. Cell. Physiol. *234*, 8327–8341. https://doi.org/10.1002/jcp.27722.

49. Palmer, E., and Freeman, T. (2004). Investigation Into the use of C- and N-terminal GFP Fusion Proteins for Subcellular Localization Studies Using Reverse Transfection Microarrays. Comp. Funct. Genom. *5*, 342–353. https://doi.org/10.1002/cfg.405.

50. Szklarczyk, D., Gable, A.L., Lyon, D., Junge, A., Wyder, S., Huerta-Cepas, J., Simonovic, M., Doncheva, N.T., Morris, J.H., Bork, P., et al. (2019). STRING v11: protein-protein association networks with increased coverage, supporting functional discovery in genome-wide experimental datasets. Nucleic Acids Res. *47*, D607–D613. https://doi.org/10.1093/nar/gky1131.

51. La Verde, V., Dominici, P., and Astegno, A. (2017). Determination of Hydrodynamic Radius of Proteins by Size Exclusion Chromatography. Bio. Protoc. *7*, e2230. https://doi.org/10.21769/BioProtoc.2230.

52. Ribbeck, K., and Görlich, D. (2001). Kinetic analysis of translocation through nuclear pore complexes. EMBO J. *20*, 1320–1330.

53. Kelich, J.M., Ma, J., Dong, B., Wang, Q., Chin, M., Magura, C.M., Xiao, W., and Yang, W. (2015). Super-resolution imaging of nuclear import of adeno-associated virus in live cells. Mol. Ther. Methods Clin. Dev. *2*, 15047.

54. Li, Y., Luo, W., and Yang, W. (2018). Nuclear Transport and Accumulation of Smad Proteins Studied by Single-Molecule Microscopy. Biophys. J. *114*, 2243–2251. https://doi.org/10.1016/j.bpj.2018.03.018.

55. Grünwald, D., and Singer, R.H. (2010). In vivo imaging of labelled endogenous β-actin mRNA during nucleocytoplasmic transport. Nature *467*, 604–607.

56. Goryaynov, A., and Yang, W. (2014). Role of Molecular Charge in Nucleocytoplasmic Transport. PLoS One *9*, e88792. https://doi.org/10.1371/journal.pone.0088792.

57. Rabut, G., Doye, V., and Ellenberg, J. (2004). Mapping the dynamic organization of the nuclear pore complex inside single living cells. Nat. Cell Biol. *6*, 1114–1121. https://doi.org/10.1038/ncb1184.

58. Tu, L.C., and Musser, S.M. (2011). Single molecule studies of nucleocytoplasmic transport. Biochim. Biophys. Acta *1813*, 1607–1618. https://doi.org/10.1016/j.bbamcr.2010.12.011.

59. Kelich, J., Yu, J., and Yang, W. (2018). Structure and Function of the Nuclear Pore Complex Revealed by High-Resolution Fluorescence Microscopy. In Nuclear-Cytoplasmic Transport, W. Yang, ed. (Springer International Publishing), pp. 249–274. https://doi.org/10.1007/978-3-319-77309-4_11.

60. Junod, S.L., Kelich, J.M., Ma, J., and Yang, W. (2020). Nucleocytoplasmic transport of intrinsically disordered proteins studied by high-speed super-resolution microscopy. Protein Sci. *29*, 1459–1472. https://doi.org/10.1002/pro.3845.

61. Kowalczyk, S.W., Kapinos, L., Blosser, T.R., Magalhães, T., van Nies, P., Lim, R.Y.H., and Dekker, C. (2011). Single-molecule transport across an individual biomimetic nuclear pore complex. Nat. Nanotechnol. *6*, 433–438. https://doi.org/10.1038/nnano.2011.88.

62. Kubitscheck, U., Grünwald, D., Hoekstra, A., Rohleder, D., Kues, T., Siebrasse, J.P., and Peters, R. (2005). Nuclear transport of single molecules : dwell times at the nuclear pore complex. J. Cell Biol. *168*, 233–243. https://doi.org/10.1083/jcb.200411005.

63. Yang, W., Gelles, J., and Musser, S.M. (2004). Imaging of single-molecule translocation through nuclear pore complexes. Proc. Natl. Acad. Sci. USA *101*, 12887–12892. https://doi.org/10.1073/pnas.0403675101.

64. Wild, T., Horvath, P., Wyler, E., Widmann, B., Badertscher, L., Zemp, I., Kozak, K., Csucs, G., Lund, E., and Kutay, U. (2010). A protein inventory of human ribosome biogenesis reveals an essential function of exportin 5 in 60S subunit export. PLoS Biol. *8*, e1000522.

65. Peabody, D.S. (2003). A Viral Platform for Chemical Modification and Multivalent Display. J. Nanobiotechnology *1*, 5. https://doi.org/10.1186/1477-3155-1-5.

66. Rabe, B., Vlachou, A., Panté, N., Helenius, A., and Kann, M. (2003). Nuclear import of hepatitis B virus capsids and release of the viral genome. Proc. Natl. Acad. Sci. USA *100*, 9849–9854. https://doi.org/10.1073/pnas.1730940100.

67. Oeffinger, M., Dlakić, M., and Tollervey, D. (2004). A pre-ribosome-associated HEAT-repeat protein is required for export of both ribosomal subunits. Genes Dev. *18*, 196–209. https://doi.org/10.1101/gad.285604.

68. Trotta, C.R., Lund, E., Kahan, L., Johnson, A.W., and Dahlberg, J.E. (2003). Coordinated nuclear export of 60S ribosomal subunits and NMD3 in vertebrates. EMBO J. *22*, 2841–2851. https://doi.org/10.1093/emboj/cdg249.

69. Katahira, J., Dimitrova, L., Imai, Y., and Hurt, E. (2015). NTF2-like domain of Tap plays a critical role in cargo mRNA recognition and export. Nucleic Acids Res. *43*, 1894–1904. https://doi.org/10.1093/nar/gkv039.

70. Katahira, J., Strässer, K., Podtelejnikov, A., Mann, M., Jung, J.U., and Hurt, E. (1999). The Mex67p-mediated nuclear mRNA export pathway is conserved from yeast to human. EMBO J. *18*, 2593–2609. https://doi.org/10.1093/emboj/18.9.2593.

71. Paci, G., Zheng, T., Caria, J., Zilman, A., and Lemke, E.A. (2020). Molecular determinants of large cargo transport into the nucleus. Elife *9*, e55963. https://doi.org/10.7554/eLife.55963.

72. Schindelin, J., Arganda-Carreras, I., Frise, E., Kaynig, V., Longair, M., Pietzsch, T., Preibisch, S., Rueden, C., Saalfeld, S., Schmid, B., et al. (2012). Fiji: an open-source platform for biological-image analysis. Nat. Methods *9*, 676–682. https://doi.org/10.1038/nmeth.2019.

73. Van Rossum, G., and Drake, F.L., Jr. (1995). Python Reference Manual (Centrum voor Wiskunde en Informatica Amsterdam).

74. Etheridge, T.J., Carr, A.M., and Herbert, A.D. (2022). GDSC SMLM: Single-molecule localisation microscopy software for ImageJ [version 1; peer review: 1 approved]. Wellcome Open Res. *7*, 241. https://doi.org/10.12688/wellcomeopenres.18327.1.

75. la Cour, T., Kiemer, L., Mølgaard, A., Gupta, R., Skriver, K., and Brunak, S. (2004). Analysis and prediction of leucine-rich nuclear export signals. Protein Eng. Des. Sel. *17*, 527–536. https://doi.org/10.1093/protein/gzh062.

76. Xu, D., Marquis, K., Pei, J., Fu, S.C., Cağatay, T., Grishin, N.V., and Chook, Y.M. (2015). LocNES: a computational tool for locating classical NESs in CRM1 cargo proteins. Bioinformatics *31*, 1357–1365. https://doi.org/10.1093/bioinformatics/btu826.

77. Doncheva, N.T., Morris, J.H., Gorodkin, J., and Jensen, L.J. (2019). Cytoscape StringApp: Network Analysis and Visualization of Proteomics Data. J. Proteome Res. *18*, 623–632. https://doi.org/10.1021/acs.jproteome.8b00702.

78. Li, Y., Junod, S.L., Ruba, A., Kelich, J.M., and Yang, W. (2019). Nuclear export of mRNA molecules studied by SPEED microscopy. Methods *153*, 46–62. https://doi.org/10.1016/j.ymeth.2018.08.005.

79. Wing, C.E., Fung, H.Y.J., and Chook, Y.M. (2022). Karyopherin-mediated nucleocytoplasmic transport. Nat. Rev. Mol. Cell Biol. *23*, 307–328. https://doi.org/10.1038/s41580-021-00446-7.

STAR★METHODS

KEY RESOURCES TABLE

REAGENT or RESOURCE	SOURCE	IDENTIFIER
Bacterial and virus strains		
NEB® 5-alpha Competent E. coli (High Efficiency)	New England BioLabs	Cat #: C2987
BL21(DE3) Competent E. coli	New England BioLabs	Cat #: C2527
Chemicals, peptides, and recombinant proteins		
Leptomycin B (LMB)	Enzo Life Sciences	ALX380100C100;CAS: 87081-35-4
SB 431542	Tocris Bioscience	Cat#1614; CAS: 301836-41-9
TransIT®-LT1 Transfection Reagent	Mirus	Cat #MIR2300
Lipofectamine 2000	Invitrogen	Cat #11668019
Tap (NXF1) – Alexa Fluor 647	Ma et al.[21]	https://doi.org/10.1038/ncomms3414
p15 (NXT1)	Ma et al.[21]	https://doi.org/10.1038/ncomms3414
Rrp12 – Alexa Fluor 647	This paper	N/A
CRM1 – Alexa Fluor 647	Ma et al.[21]	https://doi.org/10.1038/ncomms3414
ImpB1 – Alexa Fluor 647	Ma et al.[20]	https://doi.org/10.1073/pnas.1201724109
ImpB2 – Alexa Fluor 647	Ma et al.[20]	https://doi.org/10.1073/pnas.1201724109
IBB-2xMBP-M3	Ribbeck et al.[52]	N/A
Deposited data		
Canaidate single-molecule 2D localizations	Weidong Yang Lab GitHub Website	https://github.com/YangLab-Temple
Experimental models: Cell lines		
Mammailian: Pom121-GFP HeLa	Weidong Yang Lab Temple University	RRID:CVCL_A9H3
Mammailian: WT HeLa	ATCC	CCL-2
Recombinant DNA		
Plasmid: RPL3-GFP	This paper	N/A
Plasmid: RPL23-mCherry	This paper	N/A
Plasmid: RPS13-GFP	This paper	N/A
Plasmid: RPS11-mCherry	This paper	N/A
Plasmid: SMAD2-GFP	Li et al.[54]	https://doi.org/10.1016/j.bpj.2018.03.018
Plasmid: SMAD4-mCherry	Li et al.[54]	https://doi.org/10.1016/j.bpj.2018.03.018
Plasmid: GFP	Ma et al.[20]	https://doi.org/10.1073/pnas.1201724109
Plasmid: CRM1-GFP	Ma et al.[21]	https://doi.org/10.1038/nsmb.3174
Plasmid: Cripser/Cas9 (Rrp12 KO)	This paper	N/A
Software and algorithms		
ImageJ Fiji	Schindelin et al.[72]	https://doi.org/10.1038/nmeth.2019
Python	Van Rossum et al.[73]	N/A
GDSC SMLM (ImageJ Plugin)	Etheridge et al.[74]	https://doi.org/10.12688/wellcomeopenres.18327.1
OriginPro 2019a	OrginLabs	N/A
NetNES 1.1	La Cour et al.[75]	https://doi.org/10.1093/protein/gzh062
LocNES	Xu et al.[76]	DOI:
STRING software v. 11	Szklarczyk et al.[50]	https://doi.org/10.1093/nar/gky1131
Cytoscape StringApp	Doncheva et al.[77]	https://doi.org/10.1021/acs.jproteome.8b00702

RESOURCE AVAILABILITY

Lead contact

Further information and requests for resources and reagents should be directed to and will be fulfilled by the Lead Contact: Weidong Yang, weidong.yang@temple.edu.

Material availability

This study did not generate any new material.

Data and code availability

- All python[73] code and single-molecule localization data from candidiates used in this study are publically available at the Weidong Yang Lab GitHub repository (https://github.com/YangLab-Temple).
- Any additional information required to reanalyze the data reported in this paper is available from the lead contact upon request.

EXPERIMENTAL MODEL AND SUBJECT DETAILS

Cell lines

Live HeLa cells stably expressing POM121 conjugated to GFP at the C terminus (RRID:CVCL_A9H3) for single-molecule microscopy experiments and live wild type HeLa (ATCC, CCL-2) for confocal experiments.

METHOD DETAILS

Cell culture and protein expression

Experiments on pre-60s and pre-40s nuclear export were conducted in live HeLa cells (American Type Culture Collection) stably expressing POM121 conjugated to GFP at the C terminus (RRID:CVCL_A9H3). Cells were incubated with 5% CO_2 at 37°C in DMEM (Gibco) with 10% (v/v) FBS (Gibco), and 1% (v/v) penicillin-streptomycin (10,000 U/mL, Gibco). Cells were co-transfected or singly transfected with plasmids containing the open reading frame for rpL3-GFP and rpl23-mCherry, or rpS11-GFP and rpS13-mCherry. A secondary FRET pair, rpS19-GFP and rpS25-mCherry, was used to confirm the results of pre-40S. GFP tagged Imp β1 or Crm1 were transfected to the HeLa cells and single-molecule tracking of Imp β1 or Crm1 through the NPCs was conducted after completely photobleaching the fluorescence of GFP-Pom121 in the NPCs of live cells. These single-molecule experiments in live cells were conducted 24 hours after transfection.

For microscopy imaging in permeabilized cells, flow chambers were constructed with a top cover-slip and two lines of silicone grease as spacers. Cells were washed with transport buffer (20mMHEPES, 110 mM KOAc, 5 mM NaOAc, 2 mM MgOAc, 1 mM EGTA, pH 7.3), permeabilized for two minutes with 40 μg/mL digitonin in transport buffer and washed again with transport buffer supplemented with 1.5% polyvinylpyrrolidone (PVP; 360 kDa). PVP was included in all transport buffer solutions after digitonin treatment to prevent osmotic swelling of the nuclei. Nuclear transport assays for transport receptors CRM1, Tap-p15, and nuclear export adaptor Rrp12 were conducted in digitonin-permeabilized cells supplemented with 1.5% polyvinylpyrrolidone (PVP; 360 kDa). Import assays for IBB-2xMBP-M3 were conducted similarly to the transport receptor assays in digitonin-permeabilized cells. Concentrations used for all fluorescently labeled molecules were ~0.1 nM.

For live cell leptomycin B experiments, incubations were done at 37°C for 3 hours prior to imaging at the concentrations listed in the main text. We used a three-hour incubation time of LMB, which falls within the typical range of one to four hours, to achieve efficient inhibition of CRM1 while minimizing off-target effects and cellular toxicity.

Controlled expression level of acceptors for single-molecule tracking experiments in live cells

Transfection conditions were optimized through titration to achieve a lower molar concentration of mCherry acceptor labeled r-proteins in living Hela cells. 0.8 μg of plasmid DNA was utilized for mCherry containing r-proteins RpL23 and RpS13 compared to 1.2 μg of plasmid DNA used for the GFP donor labeled RpL3 and RpS11. Transfection was achieved using the transfection reagent, TransIT LT-1 (Mirus Bio), at a 1 μg plasmid DNA to 2 μL transfection reagent ratio. Similarly, 1.0 μg of plasmid DNA containing GFP labeled CRM1 was transfected using TransIT LT-1 into HeLa cells stably expressing POM121

conjugated to mCherry at the C terminus for control experiments. Detailed protocol for nuclear export of Smad proteins can be found at the subsection titled "Materials and Methods for Nucleocytoplasmic Transport of Smad Proteins in Live Cells".

Optical setup of SPEED microscopy and FRET visualization of pre-60S and pre-40S

The optical setup of SPEED technique has been described in previously published articles.[19,20,41,78] In short, the microscope is an Olympus IX81 equipped with a 1.4-NA 100× oil-immersion apochromatic objective (UPLSAPO 100×, Olympus), a 120-mW ArKr tunable ion laser (Melles Griot), an on-chip multiplication gain charge-coupled-device camera (Cascade 128+, Roper Scientific) and the Slidebook software package (Intelligent Imaging Innovations) for data acquisition and processing. 488nm, 561nm and 633nm lasers were utilized to excite either GFP, mCherry and Alexa Fluor 647 respectively. To capture FRET emissions, a dichroic mirror (506 long pass) and an emission filter (595 Long pass) were utilized. For dual-channel FRET tracking, a DV2 system (Photometrics) was used to split GFP and mCherry signal for simultaneous detection on the same CCD camera using the filters sets mentioned above. A background subtraction was conducted using ImageJ for each channel and intensity values were normalized for each channel per individual video. To avoid any possibility of POM121-GFP acting as a donor in FRET, the fluorescence of POM121-GFP is photobleached just before single-molecule detection of FRET signal in all our experiments using a high laser power of 5 mW. Immediately following photobleaching, a few seconds, the optical setup is switched to the candidates imaging parameters and imaged. Imaging of the single NPC is performed over 1-2 minutes with a standard video being ~30 seconds to account for the possibility of cellular drift.

The localization precision for fluorescent NPCs and particles

For NPCs labeled by POM121-GFP, the fluorescent spots were fitted to a 2D elliptical Gaussian function, and the localization precision was determined by the s.d. of multiple measurements of the centroid position. However, for moving molecules such as pre-ribosomal subunits, the diffusion of the particle during image acquisition must be accounted. The localization precision for moving substrates (σ) was determined by the algorithm $\sigma = \sqrt{F\left[\frac{16(s^2+a^2/12)}{9N}+\frac{8\pi b^2(s^2+a^2/12)^2}{a^2N^2}\right]}$, where F is equal to 2, N is the number of collected photons, a is the effective pixel size of the detector, and b is the s.d. of the background in photons per pixel, and $s = \sqrt{s_0^2+\frac{1}{3}D\Delta t}$, where s_0 is the s.d. of the point spread function in the focal plane, D is the diffusion coefficient of substrate in the NPC, and Δt is the image acquisition time.[41,54,78] For localizing the GFP-NPC centroid, repeated measurements generate precisions for the centroid of a single NPC with 1-3 nm precision in permeabilized cells and 5-11 nm in living cells based of the standard deviations obtained during our single-molecule tracking experiments. For moving molecules through the NPCs captured within ~300 nm in the focal plan, the localization precision is calculated to be based on the above equations and the parameters determined experimentally (a=240 nm, $b \approx 2$, s_0=150 $\pm$ 50 nm, D is in the range of 0.1 – 0.8 $\mu m^2/s$ for the tested substrates). For the Alexa-dye-labeled transport receptors in permeabilized cells, the localization precision was determined to be < 10 nm. For the FRET signal of pre-ribosomal subunits in single-channel setup, the localization precision was calculated to range from 15-35 nm.

Quantification of export efficiency

Using the plugin GDSC SMLM[74] for Fiji,[72] single molecule localizations were fit. These single molecule fittings are zero normalized and subsequently evaluated for successful or abortive export by overlying them with the localized centroid of the NPC. A successful event is defined as a contiguous trace initiating within the nucleoplasm (<-100 nm from the central plane of the NPC), passing through the NPC scaffold region, and terminating within the cytoplasm (>70 nm from the central plane of the NPC). An abortive event is defined as a contiguous trace originating within the nucleoplasm, entering the NPC and then returning to, and terminating in, the nucleoplasm. All other observed events are adjudicated as incomplete and discounted from further analysis as the most probable cause of an incomplete trace is photobleaching of the fluorophore or movement out of the focal plane. Export efficiency is defined as $Export\ Efficiency = \frac{successful\ export\ events}{successful+abortive\ events}$. A typical 30-second video, with a temporal resolution of 2ms, yields approximately 10-30 complete events, and 2-4 videos are required for a single NPC. For a detailed protocol, please refer to Nature Protocols.[41]

Epi-fluorescence microscopy imaging of LMB-dependent subcellular distributions of pre-ribosomal particles

Wild type HeLa cells were co-transfected with either RpL3-GFP and RpL23-mCherry or RpS13-GFP and RpS11-mCherry to visualize pre60S or pre40S, respectively. Live cells were incubated with titrated concentrations of LMB (0 nM, 10nM, 20nM, 40nM and 200 nM) at 37°C for 3 hours before fixation. To prepare for imaging, the transfected HeLa cells were fixed using a 1% paraformaldehyde solution for 10 minutes. Imaging was conducted using a microscope with a 1.0 NA 60X Olympus water dipping objective and a Mercury lamp with the previously mentioned FRET filtered sets. The cytoplasmic and nuclear membranes were selected using bright-field images and the ImageJ particle picker plugin. The mean FRET intensity from the cytoplasm or nucleus of individual cells was analyzed and compared under various LMB concentrations.

Protein purification and labeling

All purified proteins were expressed in *E. coli* cells (NEB, BL21 (DE3) cells) using a 6X histidine tag and purified through Ni-NTA Superflow (Qiagen) and by size exclusion chromatography (UltiMate 3000 HPLC Thermo Scientific). Alexa Fluor 647 maleimide dye (Invitrogen) was used to label proteins at surface cysteine residues. Cysteines were reduced for 30 minutes with excess of TCEP (tris-carboxyethylphosphine) in 100X molar excess. Then Alexa647 maleimide dye was introduced for 2 hours in 50 mM sodium phosphate, 150 mM NaCl with pH 7.5. To quench the reaction beta-mercaptoethanol was applied. Free dye was extracted through centrifugal filtration. The final labeling ratio was determined to be 0.7 Alexa Fluor 647 per Rrp12 molecule. For IBB-2xMBP-M3 the labeling ratio was 1.2 Alexa Fluor 647 per protein molecule. Tap-p15 had a labeling ratio of 2.2:1 and CRM1 had a labeling ratio of 1:1.

Materials and methods for nucleocytoplasmic transport of Smad proteins in live cells

We used cDNAs of RFP-Smad2 and EGFP-Smad4, which were gifts from Ali H. Brivanlou (Rockefeller University, New York, USA) and Xiaohong Fang (Chinese Academy of Sciences, Beijing, China), respectively. HeLa wild-type (WT) cells were obtained from the American Type Culture Collection and cultured in DMEM (ThermoFisher) supplemented with 10% Fetal bovine serum (FBS) and 1% Penicillin-streptomycin (PS). Our earlier publication[41] described the cell line stably expressing POM121-GFP. Our experimental design is to label the N-termini of Smad4 and Smad2 proteins with enhanced green fluorescence protein (EGFP) and red fluorescence protein (RFP), respectively, in live HeLa cells. Specifically, we transfected EGFP-Smad4 and RFP-Smad2 into WT Hela or Pom121-expressed Hela cells using Lipofectamine 2000 (Invitrogen) according to standard protocols. For TGF-β1 treatment, we treated C2C12 cell line and Hacat cell line with 5 ng/ml TGF-β1 (Peprotech) in OPTI-MEM (ThermoFisher) for 1 hour, as this timing shows a peak of nuclear accumulation for Smad2 and Smad4.[54] Similarly, our cells were treated with 5 ng/ml TGF-β1 in OPTI-MEM for 1 hour before imaging.

To inhibit phosphorylation of Smad and prevent Smad trimerization, we used SB-431542, which has been shown to be effective. We treated cells without stimulation of TGF-β1 with 1 μM SB431542 for 4 hours to serve as a negative control. For microscopy imaging in live-cell imaging, we replaced the medium with transport buffer (20 mM HEPES, 110 mM KOAc, 5 mM NaOAc, 2 mM MgOAc, and 1 mM EGTA, pH 7.3) for 30 mins before detection.

Our high-speed single-molecule tracking microscope included an Olympus IX81 equipped with a 1.4-NA 100× oil-immersion apochromatic objective (UPLSAPO 100×, Olympus), a 50mw 488nm semiconductor laser (Coherent OBIS), a 50mw 561nm laser (Coherent OBIS), an on-chip multiplication gain charge-coupled-device camera (Cascade 128+, Photometrics) and a Slidebook software package (Intelligent Imaging Innovations) for data acquisition and processing. EGFP and RFP were excited by 488 nm and 561 nm lasers, respectively, with the 488nm laser combined with an excitation filter (FF01-469/35, Semrock) and the 561nm laser combined with an excitation filter (FF01-531/40, Semrock). The two lasers were collimated and focused into an overlapped illumination volume in the focal plane. The green fluorescence emission was filtered by a dichroic filter (FF497-Di01, Semrock) and an emission filter (FF01-525/39, Semrock), while the red fluorescence emission was filtered by an emission filter (FF01-593/40, Semrock). The two fluorescence images were captured by the CCD camera (Cascade 128+).

For FRET measurements, a 5-mW 488nm laser was used for excitation. The donor and acceptor fluorescence were both collected by the same objective and split by a Dual View DV2 system (Photometrics), which included a dichroic mirror (565dcxr, CHROMA). The donor and acceptor channels were further filtered by

520 ± 15 nm band-pass (CHROMA) and 593 nm long-pass (FF01-593/LP-25; CHROMA) filters, respectively. The bleed-through signal of GFP and RFP signals with our band-pass filter is negligible, as the crosstalk index with the GFP-RFP pair in our setup is less than 10%. Single molecules were detected at 2ms per frame, and a 3μm diameter circle area was illuminated during the experiment. The illumination intensities at the sample plane were approximately 70 kW/cm^2 for both the 488 nm and 561 nm lasers.

STRING analysis of of protein-protein interactions between the pre-ribosomal r-proteins and accessory proteins to NTRs

To evaluate the[7] significance of protein-protein interactions between the pre-ribosomal r-proteins and accessory proteins to NTRs, CRM1, Rrp12, and Tap, a STRING analysis was conducted[50] (Figures S1 and S2). This analysis provides evidence that 47 r-proteins and 8 accessory proteins are associated with the pre-60S ribosomal subunit,[4] while 43 are associated with CRM1, 22 with Rrp12, and 23 with Tap. Of the 33 r-proteins and 4 accessory proteins associated with the pre-40S ribosomal subunit,[7] 35 were associated with CRM1, 25 with Rrp12, and 15 with Tap. As many accessory proteins may interact with the pre-ribosomal particles at some point throughout the maturation process, only accessory proteins associated with the complex prior to nuclear export, as defined by previously published cryo-EM results,[4,7] were selected.

In light of the significant interactions CRM1 has with numerous r-proteins and accessory proteins within the pre-ribosomal subunits, proteins were selected based upon the presence of the nuclear export signal (NES), the major recruitment signal of CRM1.[79] Computational analysis using NES prediction software, NetNES 1.1[78] and LocNES,[76] revealed several r-proteins and accessory proteins on the pre-60S and pre-40S subunits contained some form of NES (Table S1). False positive NES predictions were then removed. These false positives consist of a single amino acid fallaciously marked by the system as an NES to NESs located centrally within the subunits, as determined by cryo-EM.[4,7] Internally positioned NESs would be inaccessible by CRM1 and would not likely participate in CRM1-mediated nuclear export.[79] After filtering, 7 and 8 potential NESs were observed for the pre-60S and pre-40S subunits, respectively. NES-positive r-proteins for the pre-60S subunit include rpL3, rpL30, and rpL35, while NES-positive accessory proteins include eIF6, TMA16, LLPH, and NMD3 (Figure S3A). NES-positive r-proteins for the pre-40S subunit include rpS3A, rpS6, rpS16, rpS17, and rpS19, while NES-positive accessory proteins include BYSL, TSR1, and LTV1 (Figure S3B).

QUANTIFICATION AND STATISTICAL ANALYSIS

Experimental error is reported as mean ± standard error of the mean. P-values for nuclear transport assays were obtained via one-tailed, two sample binomial z-tests for proportions. They were calculated by two-sided Welch's t test for comparison with pre-ribosomal subunits. Not significant, *n.s.*, $P < 0.0001$, ****.